JOINT EUROPEAN TORUS

JET–P(92)93

W. Mandl, R.C. Wolf, M.G. von Hellermann, H.P. Summers
and JET Team

Beam Emission Spectroscopy as a Comprehensive Plasma Diagnostic Tool

Beam Emission Spectroscopy as a Comprehensive Plasma Diagnostic Tool

W. Mandl, R.C. Wolf, M.G. von Hellermann, H.P. Summers
and JET Team*

JET-Joint Undertaking, Culham Science Centre, OX14 3DB, Abingdon, UK

** See Annex*

Preprint of Paper to be submitted for publication in
Plasma Physics and Controlled Fusion

BEAM EMISSION SPECTROSCOPY AS A COMPREHENSIVE PLASMA DIAGNOSTIC TOOL

W.Mandl, R.C.Wolf, M.G. von Hellermann, H.P.Summers

Abstract

A beam of injected fast atomic hydrogen presents a superb probe for hot fusion plasmas. The neutral particles experience excitation and ionization by collisions with electrons and ions as they penetrate into a plasma. The emitted characteristic line radiation is Doppler shifted and the spectral lines are split due to motional Stark fields. Measurements of wavelength, intensity and polarization of the Balmer-alpha emission reveal information on the neutral beam, such as beam attenuation, beam-geometry, beam-divergence and species mix. Local pitch-angles and toroidal fields can be derived from the simultaneous measurement of the polarization pattern and the wavelength separation of the Stark multiplet. The implementation and application of beam emission spectroscopy as a quantitative diagnostic tool on the Joint European Torus (JET) experiment is reviewed.

1. Introduction

The potential of active beam emission spectroscopy (BES) has been pointed out in several papers in the past (Seraydarian et al. 1988, Boileau et al. 1989, von Hellermann et al. 1990, Summers et al. 1991, König et al. 1991). The polarization pattern of the motional Stark multiplet in the beam spectrum has been successfully used for the deduction of the pitch-angle of the local magnetic field (Levinton et al. 1989, Wroblewski et al. 1990), and the first local ion density fluctuations based on BES were described by Fonck et al. 1990 and Durst 1992.

It is the aim of this paper to give an overview of the the present status of BES for quantitative plasma diagnostics developed in recent years at JET. This refers in particular to the simultaneous measurement of the magnetic pitch-angle and the toroidal field strength making use both of the polarization pattern as well as the wavelength splitting of the Stark multiplet, and secondly, to the quantitative prediction of the beam emission spectrum and the deduction of local neutral beam densities from absolute calibrated intensities. The latter aspect is considered to be essential not only for a consistent analysis of impurity densities derived from charge exchange spectroscopy measurements (cf. von Hellermann et al. 1992), but also for the deduction of power deposition profiles in neutral beam heated plasmas and calculation of the beam-plasma related neutron production (Wolle et. al. 1992).

Even with sophisticated numerical neutral beam attenuation codes one is

realistically only able to calculate the absolute neutral beam density and the beam species mix up to a maximum penetration depth, where the initial injected beam is attenuated by less than one order of magnitude. This is because small uncertainties of a few percent in the plasma parameters or in the atomic cross-section data cause unacceptable accumulation of errors in the calculated local neutral density in cases of strong beam attenuation. Therefore for the diagnosis of large and/or dense plasmas, such as in the future ITER fusion device, it is necessary to support the attenuation calculation by determination of the local fast neutral density by BES. Conversely in a low density plasma or near the plasma edge of a high density plasma, the beam attenuation will be small. Then the measurement of the beam emission can be used to determine alternative parameters (assumed in the beam attenuation code) such as the electron density profile or the Z_{eff} profile.

In general, with viewing lines inclined to the beam direction, the beam emission spectrum is Doppler shifted and it is easily distinguished from the stationary hydrogen spectrum. A local measurement of the component of the total magnetic field perpendicular to the neutral beam can be obtained from the spectral shape of the Doppler shifted emission of the Balmer-alpha (H_α,D_α) line from Hydrogen or Deuterium atoms in the neutral beam. The line shows the structure of a linear Stark multiplet due to the electric Lorentz field $\vec{U}_L=\vec{v}_{beam}\times\vec{B}$ (motional Stark effect). Additional information about the direction of this field component is contained in the polarization direction of the σ- and π-components of the Stark pattern and also in their intensity ratios. Combining the information on pitch angle and wavelength splitting is sufficient to determine the absolute strength and direction of the total magnetic field if reasonable assumptions about the flux geometry are made. From the splitting of the Stark multiplet changes of 0.2% in B_{tor} are measurable. For example a diamagnetic reduction of several percent in B_{tor}, caused by fast particles driven by ICRH, can be resolved clearly. Applications of such measurements include the deduction of the relaxation time of the fast particles, their energy content, the spatial location of the RF coupling and the local power deposition. The complete determination of the magnetic field vector by BES without any independent assumptions is possible by, for example, injecting alternately two neutral beams which penetrate the observation volume at different angles.

The principal parameters which can be determined directly from the measurements and their diagnostic impact are as follows:

principal measurement		diagnostic information	
I	Doppler shift	location of observation volume (radial and vertical)	
II	intensity ratio of Stark multiplet due to the operation of offset individual beams	divergence of neutral beams	
III	spacing of Stark components	strength of Lorentz electric field	$\vec{B}\|,\vec{B}$
IV	polarization pattern of Stark components	direction of Lorentz electric field	$\vec{B}\|,\vec{B}$
V	intensity ratio of σ- to π-group	direction of Lorentz electric field	$\vec{B}\|,\vec{B}$
VI	intensity ratios of Stark components within the σ- or π-group	n=3 Stark sub state population and their redistribution	
VII	total flux of full-energy emission	local neutral particle density	
VIII	relative flux of fractional-energy emission	local mixture of fractional-energy beam components	

It is noted that all these measurements are local, yielding local parameters. This means that full radial profiles can be constructed without recourse to Abel inversion or tomography, simply by measuring at a number of different locations.

1.1 Experimental configuration and raw data analysis

Figure 1a) is a plan view of the JET tokamak, showing the neutral beam injector (NBI) assemblies at the torus octants 4 and 8. The optical head collects light along a set of nearly horizontal viewing lines intersecting the neutral beams of octant 8 (figure 1b)). A stack of quartz fibers is used to relay the light to a remote location outside the biological shield. There an assembly of spectrometers, which are fitted with 2-dimensional CCD detectors, is used to record simultaneously spectra from the different viewing lines at up to four different wavelengths. The optical head at the vacuum vessel also contains polarization sensitive elements for the magnetic field measurement. Clearly optically active components which can influence the polarization plane of transmitted light in an arbitrary way must be avoided. Vacuum windows of fused silica are found to be acceptable if

mechanical stress is avoided. For the polarization measurements the incoming light is led through an assembly of polarizing beam splitter cubes (figure 2). Once the light is separated into two orthogonal polarization components, each component is led into an optical fiber for relay, so allowing simultaneous measurement of both components. The sensitivity of the measurements to small changes in the polarization direction is maximized by inserting a half-wave plate into the optical path. By means of that plate one can rotate the incoming linearly polarized light by a defined angle in order to balance the light intensity in the two channels after the polarizers. More details concerning the polarization measurements are given in section 3.

The spectra obtained (figure 3) are approximated by a sum of Gaussians, convolved with the instrument function of the spectrometers. The fit is constrained by enforcing equi-distant spacing in wavelength and the theoretical symmetry of the Stark features. Thus the number of independent fitting parameters is reduced to equal the number of independent physical parameters required to describe the beam emission spectrum. The absolute intensities, Doppler shifts and the Stark splitting of the full, half and third energy components of the NBI as a function of the radial position are retrieved unambiguously by this method.

1.2 The emission spectrum of excited fast neutral atoms

As is well known, the injection of fast neutral deuterium atoms into a fully-ionized hot plasma leads to two physically distinct, intense Balmer-α features with high diagnostic potential (Boileau et al. 1989). The first is emission by plasma deuterium atoms, following the charge exchange reaction between neutral beams and deuterons in the bulk plasma.

$$D^{o}_{beam} + D^{+}_{plasma} \longrightarrow D^{+}_{beam} + D^{o*}_{plasma} \qquad (1.1)$$

However, in this paper we are interested in the second feature, the beam emission. This feature is excited dominantly by collisions with plasma deuterons, fully stripped impurity ions and, to a lesser extent, with electrons.

$$\begin{array}{lll} \text{deuterons:} & D^{o}_{beam} + D^{+}_{plasma} & \longrightarrow D^{o*}_{beam} + D^{+}_{plasma} \\ \text{impurity ions:} & D^{o}_{beam} + Z^{z+}_{plasma} & \longrightarrow D^{o*}_{beam} + Z^{z+}_{plasma} \\ \text{electrons:} & D^{o}_{beam} + e^{-}_{plasma} & \longrightarrow D^{o*}_{beam} + e^{-}_{plasma} \end{array} \qquad (1.2)$$

Light emitted from the neutral beams is Doppler shifted, depending on the velocity of the injected particles and on the angle between the beams and the viewing lines. The beams intersect the magnetic field lines at angles between

110 and 150° and a strong electric field is therefore experienced by the neutrals in their center of mass frame. The $\vec{v}\times\vec{B}$ Lorentz electric field perturbation causes the D_α line to split into 15 Stark components, 9 of which are usually strong enough to be observed (figure 4). Since the beam consists of three energy fractions, corresponding to the presence of D^+, D_2^+, D_3^+ in the positive ion source of the neutral beam injectors, the Stark multiplet appears three times at different Doppler shifts in the spectrum.

For studies of spectral emission by hydrogen in fusion plasma environments it is convenient to calculate directly the energy level, transition probabilities and radiation angle distributions, allowing for arbitrary orientation of magnetic field (and associated orthogonal Lorentz electric field) and an independent non-orthogonal electric field. It is sufficient to consider the $e\cdot\vec{U}\cdot\vec{r}$ and $\frac{\mu}{\hbar}(\vec{L}+2\vec{S})\cdot\vec{B}$ in first order perturbation theory on the non-relativistic isolated atom Hamiltonian. For magnetic fields of the order of a few tesla and typical beam speeds of several 10^6 m/s the maximum electric fields are ≤ 10 MV/m. Thus for principal quantum shells ≤ 4 the linear Stark effect only needs to be considered, that is interaction between states of like principal quantum number. The quadratic Stark effect becomes significant at much higher electric fields (≈ 50 MV/m). We seek convenient modeling of hydrogen in all the environments extending from the low density, beam free plasma edge where the Zeeman structure dominates to the neutral beam where almost pure Stark structure is apparent. Figures 5a and 5b show a transition from Zeeman to Stark line pattern caused by increasing the speed (energy) of injected atoms while maintaining a fixed magnetic field. For higher Lorentz field strengths the Stark pattern is plotted on a field scaled wavelength axis in order to emphasize small changes.

We have carried out detailed calculations of the formation and mixing of population of the static field basis states under ion and electron collisions (see also section 2). However it is evident that for the n=3 shell for hydrogen in the beam, the mixing is nearly complete, so that relative statistical populations of sub states are established. We have sought to validate this experimentally. The approach is to plot line ratios within the σ and π parts of the emission as a function of plasma density (figures 6 and 7). The absence of a clear density dependence supports the fully mixed hypothesis. However statistical analysis of the line ratios shows a small but statistically significant deviation from the expected value for the σ1/σ2 and π3/π4 ratios. We have no quantitative explanation for this deviation, but the discrepancy is small enough not to affect the validity for further data analysis.

It is observed that Stark components which are shifted to higher wavelengths than the field free position appear to be broader than those shifted to lower wavelengths. This can be explained as a geometrical effect induced by the angular divergence of the neutral beams.

2. Measurement of local neutral beam density and Z-eff

The intensities of all charge exchange lines are proportional to the local fast neutral particle density. For quantitative measurements, it is therefore essential to know the attenuation of the beams to the observation point. The two methods available are either direct measurement of the light emitted by exited beam atoms and deduction of the local beam density from this, or purely numerical prediction by calculating the losses as the beam penetrates the target plasma. It must be noted that the first method also requires theoretical modeling of the relationship between the emission and the ground state beam atom population.

Beams are attenuated by ionization of its individual atoms. The possible processes considered here are ionization due to electron impact, ionization due to ion impact and charge exchange reactions with plasma ions. By plasma ions we mean deuterons as well as impurity ions.

$$\begin{aligned} D + e^- &\rightarrow D^+ + e^- + e^- \\ D + Z^{Z+} &\rightarrow D^+ + e^- + Z^{Z+} \\ D + Z^{Z+} &\rightarrow D^+ + Z^{(Z-1)+} \end{aligned} \qquad (2.1)$$

In a low density plasma, only the ground state of the neutral hydrogen beam atoms is significantly populated and so ionization takes place directly from this state. The ionization rate coefficient S_1, defined in terms of the electron collisions, is given by

$$n_e S_1 = n_e S_1^{(e)} + \sum_{ion} n_{ion} (q_1^{(CX)} + S_1^{(ion)}) \qquad (2.2)$$

where the sum is over all plasma ions (deuterons and impurity ions). $S_1^{(e)}$ is the zero density ground state electron collision impact ionization coefficient, $q_1^{(CX)}$ is the charge exchange loss rate coefficient from the ground state to the plasma ion and $S_1^{(ion)}$ is the zero density ground state ion impact ionization rate coefficient.

Consequently

$$\frac{dN_1}{dl} = -n_e \cdot \frac{S_1}{v_{beam}} \cdot N_1 \qquad (2.3)$$

where N_1 is the ground state beam atom density. Commonly an 'effective' ionization cross section σ is introduced, so that $\sigma^{eff}_{ionisation} = S_1/v_{beam}$.

However, tokamak devices are usually operated at electron densities of several $10^{19}m^{-3}$. In these circumstances the excited state population of the beam atoms cannot be neglected in the attenuation process. Step-wise collisional losses through excited states occur and collisional radiative calculations are required. The excitation and deexcitation ion and electron impact reactions between bound states must be added to those above. The techniques described in earlier works (Burgess et al. 1976, Summers 1977, Summers et. al. 1983) have been used but with full inclusion of ion impact collisions. Note that the calculation of the beam emission spectrum (section 1.2) and the calculation of effective attenuation rate coefficients become one. Because of the strong mixing, the bundle-n approach is adequate for practical purposes, although the condensation and expansion techniques (Summers et al. 1992), projecting onto the Stark manifold, have been implemented for special studies. The collisional radiative calculations yield the effective 'collisional-radiative' ionization coefficient S_{CR} which replaces S_1 in equation (2.3) above. This coefficient is of course density as well as temperature dependent. Extensive look-up tables of this coefficient have been established for rapid access in attenuation calculations.

The calculations also provide the effective emission coefficients for the various emitted spectral lines such as $q_{cr}(3\rightarrow2)$ for the whole Balmer alpha super transition array. This is also expressed as an effective electron cross-section so that

$$\sigma^{eff}_{3\,2} = \frac{q_{CR}(3\rightarrow2)}{v_{beam}} \qquad (2.4)$$

and the photon flux is

$$\Phi_{3\,2} = n_e \sigma^{eff}(3\rightarrow2) v_{beam} N_b \qquad (2.5)$$

The fundamental data, processing codes and derived data base used for this paper, form part of a general approach to atomic modeling in use at JET. This is called the 'Atomic Data and Analysis Structure' ADAS (Summers et al. 1991, Summers et al. 1992).

Examples of effective emission and ionization coefficients are given in figure 8 as a function of electron density.

If the effective ionization rate by all processes of beam atoms of speed v_{beam} is S^{eff}, then defining a stopping cross-section by $\sigma^{eff}=S^{eff}/v_{beam}$, the local beam density $N_b(r)$ at a position r measured from the plasma edge is:

$$N_b(r) = N_b(0)\cdot\exp\left[-\int_0^r n_e\cdot\sigma^{eff}\cdot d\ell\right] \qquad (2.6)$$

where n_e is the electron density and $N_b(0)$ the neutral beam particle density at r=0.

Thus an error $d(n_e\cdot\sigma^{eff})$ gives an error

$$\frac{dN_b(r)}{N_b(r)} = \ln(N_b(r)/N_b(0))\cdot\frac{d(n_e\cdot\sigma^{eff})}{n_e\cdot\sigma^{eff}} \qquad (2.7)$$

in the local neutral particle density. This is a serious source of error propagation. If $(n_e\cdot\sigma^{eff})$ is known everywhere to an accuracy of 10% then the relative error on the local neutral particle density for some typical values of beam attenuation is

$N_b(r)/N_0$	80%	50%	10%	5%	1%
$dN_b(r)/N_b(r)$	2.2 %	6.9 %	23%	30%	46%

A 40 keV/amu neutral hydrogen beam is typically attenuated to 10% of its density at the plasma edge after it has penetrated 1.5 meter into a plasma with a uniform electron density of $5\cdot10^{19}m^{-3}$. In this case the sensitivity of the calculation is acceptable. For situations where the electron density is higher or where the penetration depths are larger one soon enters a regime where the accuracy of numerical attenuation codes falls below 50%.

The measurement of radiation from the neutral beams allows on the other hand a direct and local evaluation of the neutral particle density.

Our first study is the fractional energy component mix of the neutral beams. The ratio of neutral particle densities N_b can be calculated from the ratio of the measured photon fluxes Φ as

$$\frac{N_b^{frac}}{N_b^{full}} = \frac{q_{eff}^{full}}{q_{eff}^{frac}} \cdot \frac{\Phi^{frac}}{\Phi^{full}} \tag{2.8}$$

where the phrases 'full' and 'frac' are used to indicate the full and fractional energy beam components. q_{eff} are calculated effective coefficients of the Balmer-alpha emission. Local neutral density and injected Power P relate to each other by:

$$\int N_b dl = \frac{P \cdot \zeta \cdot \int f_b dl}{\pi w^2 \, E_b \cdot v_{beam}} \tag{2.9}$$

where ζ is the beam attenuation at a given location, E_b and v_{beam} are the beam energy and particle velocity, and πw^2 is the cross-section of the beam. The line integration $\int f_b dl$ through the beam profile f_b is along the line of sight. The ratio of the beam powers going into the full and fractional beam components P^{frac}/P^{full} can now be found by combining the neutral particle density measurement via beam emission spectroscopy and the predicted neutral beam attenuation ζ from the attenuation calculation.

The measurement which is displayed in figure 9 yields power ratios of:

$$\frac{P^{half}}{P^{full}} = 0.25 \quad \text{and} \quad \frac{P^{third}}{P^{full}} = 0.12$$

hence we find:

$$P^{full}:P^{half}:P^{third} = 0.73:0.18:0.09$$

This can be compared with test-bed calorimeter measurements. They yield typically $P^{full}:P^{half}:P^{third} = 0.76:0.16:0.08$. Knowing the beam energy species mix, we can now proceed to calculate the local absolute neutral beam densities with the beam attenuation code. Figure 10 shows the neutral beam density for the 40 keV/amu energy fraction as measured with beam emission spectroscopy compared with the values from the attenuation calculation. Each cluster of symbols represents measurements with a certain viewing line, the corresponding positions in the plasma are indicated.

We draw attention, in spite of the good absolute agreement between measured and expected values of the neutral density, to a systematic deviation in the outermost channels. This is not too unexpected, since a radially constant, line averaged Z_{eff} was used for the analysis. Exact agreement can be obtained by allowing Z_{eff} to vary radially. In this manner the Z_{eff} profile of figure 11 is obtained. The average Z_{eff}, calculated from the profile, is again in close absolute agreement with the line averaged value from bremsstrahlung measurements.

2.1 Divergence of the neutral beams

The spatial neutral particle density distribution is assumed to have a Gaussian profile in a plane perpendicular to the beam direction. Construction details of the beam injectors suggest a different 1/e width of this density distribution in the vertical and horizontal directions. If x and y denote the horizontal and vertical distance from the axis of the beam, the profile shape can be approximated by:

$$f_b \simeq \exp-\left(\frac{x}{d_x}\right)^2 \cdot \exp-\left(\frac{y}{d_y}\right)^2 \qquad (2.10)$$

where d_x and d_y are the half widths of the neutral particle density profile in x and y direction. The measurement is not sensitive to small variations in d_x provided $0.5 \leq d_x : d_y \leq 2$, because of the near horizontal alignment of the viewing lines.

The active observation volumes generally have different distances to the axes of the beams from the separate pinis (positive ion source neutral injector) number 1 and 8. The measured photon flux Φ from the beam emission is proportional to the electron density n_e to the injected beam power P_{NBI} and to the line integral through the normalized beam profile $\int f_b dl$ and inversely proportional to the beam attenuation ζ. We expect therefore a step in the measured line strength when pini 1 is switched off and pini 8 switched on. Figure 12 shows the quantity $\Phi \cdot \zeta / (n_e \cdot P_{NBI}) \simeq \int f_b dl$ as a function of time. The neutral particle density $\int f_b dl$ integrated along a particular viewing line is a function of the beam divergence. $\int f_b dl$ decreases by a factor of 1.87 at the change over from pini 1 to pini 8. We compare this with the expected ratio in figure 13 and deduce a vertical beam divergence of 0.57°.

If we apply the same method to the neutral particle flux of the half or third energy beam components, the values 0.79° and 0.82° are found respectively for the beam divergence. Test-bed calorimeter measurements suggest an average vertical divergence of 0.7°(±0.1°). This is in reasonable agreement with our

own results, however, knowledge of the energy dependence of the divergence is crucial for charge exchange spectroscopy, since the CX cross-sections for the different fractional energy components are very different.

3. Exploiting the Doppler shift of the signals

The Doppler shift of the beam emission can be measured with a statistical accuracy of a fraction of a percent. Systematic errors have been examined carefully. The dispersion in terms of wavelength units per detector pixel depends not only on the spectrometer but also on optical and fiber-optical components inside the detectors. Also the analysis of the measurement relies heavily on the precision with which the acceleration voltage and geometry of the NBI is known.

3.1 Determination of the location of the observation volume

The observation volume of any active neutral beam spectroscopy is given by the intersection volume of the neutral beams and the viewing line. It is usually chosen prior to plasma physics experiments. The alignment of the neutral beams and viewing lines is checked by shining a laser beam through the neutral beam ducts and the light gathering optics and then observing where it strikes a suitable screen or the vessel wall. Such tests are cumbersome as they require either vessel entry or the use of other optical in-vessel surveillance methods. More important still, mechanical stress caused by the full operating temperature and the electro-magnetic forces during plasma discharges is known to disturb the alignment of the setup temporarily or sometimes permanently in the course of the actual experiments. It is therefore important as well as convenient to be able to determine the location of the observation volume in situ.

All deductions of spatial locations from active measurements are necessarily relative to the neutral beam geometry. This is not a severe restriction, because the central axis of each neutral beam is well defined by the location of the ion source and by the port through which the beams enter the torus. In the following section the observation geometry at JET which comprises a fan of near-horizontal viewing lines will be discussed, but the basic concept is generally valid.

JET pulse #19949 is a typical discharge. In this experiment pini 1 was fired for one second and then after a gap of 0.2 seconds pini 8 was fired for one second. The signal which was measured with viewing line number 5 of the horizontal array was analyzed with our multi-Gaussian fit code. Figure 14 shows the Doppler shift of the 0σ-component of the full-energy Stark

multiplet as a function of time.

From the Doppler shifts $\Delta\lambda_D=\lambda_o \cdot v_{beam}/c \cdot \cos(\gamma)$, during the injection times of pinis 1 and 8 respectively, the intersection angles $\gamma^1 = 129.08^\circ$ and $\gamma^8 = 130.01^\circ$ between viewing line and the path of the neutral can be deduced. To interpret this result recall the geometrical layout of the system given in section 1. Pini 1 and pini 8 are the $\pm 3^\circ$ beams of the tangential injector box at torus octant 8. The observation port and optical head are located 280 mm above the mid-plane of the torus.

The observation optics are designed so that the viewing line number 5 nominally intersects the beam-line at major radius $R_{maj}=3.4$m at the torus mid-plane. That means it does not intersect the center of any of the neutral beams. Since the neutral particle density decreases with distance from the beam axis, the line integrated emission from excited beam particles is heavily weighted towards the point of closest approach between viewing line and neutral beam axis. Since the observation port is located above the torus mid-plane, there will be a different active observation volume, depending on the beam is used. Because of this and because of the different locations of the beam sources of the various beams, the intersection angle γ of a given viewing line with the fast neutrals will also depend on the beam fired. Figure 15a shows a calculation of the difference $\Delta\gamma=\gamma_8-\gamma_1$ between the intersection angles with respect to pini 1 and 8 as a function of major radius R_{BL} and vertical offset. The symmetry line of all the octant 8 neutral beams is called the 'beam-line'. The major radius R_{BL} and vertical offset H_{BL} are defined as the coordinates of the intersection point between the viewing line and a vertical plane which contains the beam-line axis.

It turns out that $\Delta\gamma$ is only a weak function of the major radius, but shows a strong dependence on the vertical offset H_{BL} of the intersection point. Figure 15b shows the radial dependence of the intersection angle γ.

The observation volume is found to be located at R_{maj}= 3.396 m, H = -0.113 m when pini 1 is fired and at R_{maj}= 3.397 m, H =-0.113 m when pini 8 is fired. R_{maj} is here the major radius and H the height above the torus mid-plane.

4. Magnetic field measurements

The dependence of the shape and intensity of the Stark multiplet on the presence of electric and magnetic fields was discussed in some detail in section 1.2. At JET we are usually concerned with beam energies in excess of 10 keV/amu and the intersection angles between neutral beams and magnetic

field lines are greater than 45°. Resolve the magnetic field $\vec{B}$ as $\vec{B} = \vec{B}_\perp + \vec{B}_\parallel$ into its two orthogonal components, $\vec{B}_\perp$ the component perpendicular to the beam velocity $\vec{v}_{beam}$ and $\vec{B}_\parallel$ parallel to $\vec{v}_{beam}$.

The magnitude of the Lorentz electric field $U_L = v_{beam} B_\perp$ gives the fundamental Stark splitting interval $\Delta\lambda$ of the Balmer-alpha line

$$\Delta\lambda = \frac{3}{2} \frac{e\ a_o}{h\ c} \lambda_o^2\ U_L \qquad (4.1)$$

where e = electron charge, a_o = Bohr radius, h = Planck constant, c = speed of light, λ_o = wavelength of transition without external fields.

Thus the measurement of the Stark splitting $\Delta\lambda$ allows the determination of $B_\perp$ only. The direction of the component $\vec{B}_\perp$ relates to $\vec{U}_L$ as

$$\vec{B}_\perp = \frac{\vec{U}_L \times \vec{v}_{beam}}{v_{beam}^2} \qquad (4.2)$$

There are two principal methods to determine the direction of the electric field vector $\vec{U}_L$. The first method makes use of the different angular distributions of σ- and π-Stark components emission relative to the electric field direction. The other is to measure the polarization of the radiation.

The irradiance from σ- and π-components of the Stark multiplet is anisotropic. With θ the angle between electric field vector and viewing line, the polar distribution is

$$\Phi_\pi \sim \sin^2(\theta); \qquad \Phi_\sigma \sim 1+\cos^2(\theta) \qquad (4.3)$$

The Stark energy levels of the n=3 shell are believed to bestatistically populated at electron densities of several 10^{19} m^{-3}. However, the relative line ratios within the σ- or π-patterns were found to deviate slightly from the expected values. This could affect the ratio of total σ- to total π-emission, however, we have no indication that this is the case. We assume:

$$\frac{\Phi_\pi}{\Phi_\sigma} = \frac{\sin^2(\theta)}{1+\cos^2(\theta)} \qquad (4.4)$$

Consequently θ becomes:

$$\theta = \arctan\left(\pm \frac{2 \cdot \Phi_\pi}{\Phi_\sigma - \Phi_\pi} \right) \tag{4.5}$$

In this context we note that the field strength U_L and the angle θ determine the electric field vector $\vec{U}_L$ completely.

It is apparent that there is no information on $\vec{B}_\parallel$ from a single measurement of the Stark emission, as the component $\vec{B}_\perp$ alone determines the electric field $\vec{U}_L$. However, if the same observation volume is penetrated by neutrals which come from two different sources a and b with nonparallel velocity vectors $\vec{v}^a$ and $\vec{v}^b$, the full magnetic field vector $\vec{B}$ can be measured.

Assume that neutral particle sources a and b are fired alternately, so that we are able to measure the separate electric fields $\vec{U}_L^a$ and $\vec{U}_L^b$:

$$\vec{U}_L^a = \vec{v}^a \times \vec{B}; \qquad \vec{U}_L^b = \vec{v}^b \times \vec{B} \tag{4.6}$$

Expressing these two equations in their cartesian components we obtain a soluble set of linear equations for the components of the magnetic field vector $\vec{B}$.

Magnetic fields in tokamaks are customarily expressed in terms of their toroidal and poloidal components, that is as

$$B_{tor} = \vec{B} \cdot \vec{t}; \qquad |\vec{B}|^2 = B_{pol}^{\ 2} + B_{tor}^{\ 2} \tag{4.7}$$

where $\vec{t}$ is the unit vector in toroidal direction.

Consider again JET pulse #19949. Statistical analysis of the temporal evolution of the angle θ during operation of pini 1 and pini 8 respectively yields:

pini 1: $\theta = 64.9^\circ \pm 1.7^\circ$
pini 8: $\theta = 63.9^\circ \pm 2.5^\circ$

To deduce the magnetic field vector from these values, we first evaluate the electric field vectors during injection of the individual neutral beams, obtaining:

$$B = 2.63\ T$$
$$B_{tor} = 2.52\ T$$
$$B_{pol} = 0.74\ T$$

This is to be contrasted with the results from the magnetic equilibrium code (IDENTC):

$$B = 2.99\ T$$
$$B_{tor} = 2.96\ T$$
$$B_{pol} = 0.41\ T$$

The example demonstrates the broad feasibility of the method. The difference of 0.3 tesla between measured and predicted values is, however, unacceptable high. The main problem in the analysis is the measurement of the angle θ between viewing line and the magnetic field vector by comparing the photon flux from σ- and π-components. There are two potential error sources. First, there is the statistical relative population assumption discussed in section 1.2. Secondly we assume the diagnostic system to have the same sensitivity for σ- and π-polarized light. This assumption is insecure, because the optical chain involves a mirror as the first element facing the plasma. We expect only marginal differences in the reflection coefficients for π and σ components of the nominal aluminum coated nickel mirror, but additional coatings resulting from random deposition of undefined layers from the plasma environment may worsen this.

Inverting this argument, the magnetic field vector, as returned from the equilibrium code, allows the calculation of the expected σ/π intensity ratio. Comparison with the measured line ratio suggests that the reflectivity of the aluminum mirror was reduced by about 24% for σ-components relative to π-components in pulse #19949.

Direct measurement of the polarization direction of π- and σ-components reduces these difficulties. Polarizing elements acting as analyzers have been installed inside the optical head, which is facing the plasma (figure 2). They have to be placed in front of the optical fibers, since multi-reflections occurring in optical fibers average out most of the polarization information. The chosen detection technique allows simultaneous

measurement of the polarization angles while still retaining the full spectral resolution for measuring the Stark splitting. Thus the full Lorentz electric field (both orientation and magnitude) may be obtained.

The polarization pattern of the Stark multiplet is reflected in the irradiance described above. The π-component is linearly polarized parallel to the Lorentz field and the σ-component perpendicular to the Lorentz field. There is an additional unpolarized contribution. By taking the intensity ratios in the two polarization channels of the π- or σ-components respectively, the orientation of the Lorentz electric field may be determined:

$$\tan^2\alpha_\pi = \frac{I_1^\pi}{I_2^\pi}, \quad \tan^2\alpha_\sigma \approx \frac{I_1^\sigma}{I_2^\sigma} \tag{4.8}$$

where α_π, α_σ are the polarization angles relative to the analyzers.

The $\approx$ reflects the fact, that the unpolarized contribution of the σ-component, which depends on the viewing angle relative to the Lorentz field, introduces an error of $< \pm 0.5^\circ$ on α_σ. Neglecting the unpolarized background one obtains $\alpha_\pi = \alpha_\sigma - 90^\circ$, which means that α_π and α_σ evolve in anti-phase. Comparing α_π and α_σ therefore allows discrimination of spurious effects.

Both α_π and α_σ are a direct measure of the pitch angle, defined as the angle between the total magnetic field and the toroidal direction.

Unpolarized light, such as bremsstrahlung or the total beam emission (the sum over all π- and σ-components) can be used to check the relative calibration of related polarization channels in situ during plasma operation. Information on spurious polarization effects such as Faraday rotation in the viewing optics or the influence of the mirror on the measured polarization direction is obtained by injecting neutral beams into the tokamak filled with cold deuterium gas only. Thus with no plasma current, the known vacuum toroidal field delivers an absolute calibration of the polarization angles.

In figure 16 an example of a radial poloidal magnetic field profile using the polarization measurement described above is compared with the result obtained by an Abel inverted profile of the Faraday rotation angles measured by the far infrared interferometer (O'Rourke et al. 1992, Soltwisch et al. 1992). The offset between the measurements, which lies outside the statistical error

margins, must be attributed to the influence of the mirror on the polarization direction. In figure 17 the polarization angles of π- and σ-components during a "monster sawtooth" crash are shown. The observed angles change by $\approx 0.3^{\circ}$, which is equivalent to a poloidal magnetic field decrease of -0.024 T. Anti-correlation between the angles obtained from the two components can be seen clearly.

Magnetic equilibrium codes usually evaluate the toroidal component of the magnetic field much more accurately than the poloidal component. It is therefore a valuable consistency check to calculate B_P using the magnitude of the measured electric Lorentz field U_L and the toroidal magnetic field component B_T from the equilibrium code and to compare it with the poloidal magnetic field component which is returned by the equilibrium code.

B_P may then be expressed as a function of the measured Lorentz electric field U_L:

$$B_p = \frac{\hat{v}_p \hat{v}_t}{1 - \hat{v}_p^2} \cdot B_t \pm \left(\frac{\hat{v}_p^2 \hat{v}_t^2 - (1 - \hat{v}_p^2)(1 - \hat{v}_t^2)}{(1 - \hat{v}_p^2)^2} \cdot B_t - \frac{U_L^2}{(1 - \hat{v}_p^2)^2 v^2} \right)^{1/2} \tag{4.9}$$

where $\hat{v}_p = \frac{\vec{v}_{beam}}{v_{beam}} \vec{p}$, $\hat{v}_t = \frac{\vec{v}_{beam}}{v_{beam}} \vec{t}$ ($\vec{p}$, $\vec{t}$: unit vectors in poloidal, toroidal direction).

The ambiguous $\pm$ sign reflects the fact that we are not able to detect any difference between anti-parallel magnetic field vectors. Which sign has to be used depends on the specific geometry in a given case and has to be decided upon by means of additional information such as symmetry arguments. An example for such a B_p profile is shown in figure 18.

The error bars on our measured values are not statistical uncertainties of individual measurements, but indicate the range which is covered by a sequence of measurements during neutral beam injection. The statistical uncertainty on individual measurements of the Stark splitting is usually less than 1%. This indicates the presence of time variations of the local magnetic field, in particular of its toroidal component, which are not detected by the magnetic equilibrium code. As a results the deduced poloidal field shows an apparent temporal variation which is not present on the poloidal field from the code. The observation that the deduced poloidal field from the Stark splitting nevertheless agrees with the poloidal field from the equilibrium

code demonstrates the high accuracy of the measurement of the Stark splitting.

The measurement of the polarization angles of the Stark multiplet allows to resolve small changes of the pitch angle. The simultaneous monitoring of the Stark splitting, which is most sensitive to toroidal magnetic field changes, yields information about the toroidal field.

Measuring small toroidal field changes of less 1% one has to ensure that no other spurious effects contribute significantly. In this context one of the main concerns are the spatial stability of the observation positions and the constancy of the acceleration voltage of the neutral beam injectors. The time evolution of the Doppler shift shows small fluctuations only. This is interpreted as radial movements of the centers of the observation positions relative to the neutral beams of $\Delta R < 2.5$ mm or as velocity changes of $\Delta v/v < 0.1\%$. The contribution of the local poloidal field to the measured effect, most of it caused by a Shafranov shift due to ICRH (radial movement of the magnetic axis < 5 cm), can be neglected as well. A decrease of the spatially resolved toroidal magnetic field induced by ICRH of the order of 0.5% to 4.0% has been observed (figure 19). The maximum change is seen at the location of the ICRH resonance layer. The effect is explained by a diamagnetic drop of the magnetic field caused by the increase of plasma energy due to ICRH heating.

5. Summary and conclusions

Beam-Emission-Spectroscopy (BES) has developed over the last view years into a very versatile plasma diagnostic tool. In this paper we have given an overview on the quantitative use of BES in terms of precise local magnetic field measurements, neutral beam deposition profiles and the deduction of beam parameters such as beam divergence and species mix.

The close link to active charge exchange spectroscopy (CXS) and the deduction of local impurity densities which depends crucially on the determination of the local beam strength has been discussed. A consistent treatment of the neutral beam attenuation process in a plasma shows indeed that BES and CXS are inseparable, and that for understanding of the observed line strength in the beam spectrum a comprehensive description of radial impurity density profiles, and hence a profile of the effective ion charge, is required, which ultimately can be retrieved from BES measurements. In addition to a complex atomic description of the excitation mechanism and its parameter dependence we have established that the accurate description of the beam and observation geometry play a vital role for the deduction of local parameters.

The overall conclusion is therefore that the combination of BES and CXS has extended the confidence in the reliability of impurity density and beam deposition profile measurements. The prospect of applying quantitative CXS methods in present and future high density plasmas, where beam stopping is relevant, are therefore considerably improved.

We have tried to emphasize the fact that magnetic field measurements based on the motional Stark effect usually provide only a subset of a three-dimensional magnetic field vector. Only if either certain symmetries can be assumed or alternatively the measurement of pitch angles can be combined with measurements of absolute Lorentz fields, it is possible to derive a unique description of the local field. The ultra precise measurement of the Lorentz field in the plasma core appears to be a very promising tool for the assessment of minute changes in the central toroidal field and hence changes of the plasma pressure.

6. Acknowledgements

We wish to thank W. Engelhard and P. Thomas for their continuous encouragement and support from the very start of the beam emission spectroscopy at JET.

References

Boileau A., von Hellermann M., Mandl W., Weisen H., Zinoviev A. (1989), J. Phys. B **22**, L145

Burgess A., Summers H. P. (1976), Mon. Not. R. Astr. Soc., **174**, 345

Durst D. (1992), Fonck R., Cosby B., Evensen H., Rev. Sci. Instr. **63**, 4907

Fonck R. J. (1990), Rev. Sci. Instr. **61**, 3070

von Hellermann M., Mandl W., Summers H. P., Weisen H., Boileau A., Morgan P., Morsi H., König R., Wolf R. (1990), Rev. Sci. Instr. **61**, 3479

von Hellermann M., Summers H. P. (1992), Rev. Sci. Instr. **63**, 5132

O'Rourke J., Edwards A. W., von Hellermann M., Wolf R. (1992), Proc. Am. Phys. Soc.

König R., Summers H. P., von Hellermann M., Mandl W., Frieling J., Horton L. D., Breger P., Morsi H., Wolf R., Proc. Workshop on Diagnostics for Contemporary Fusion Experiments, Varenna, Sept. 1991, p. 925

Levinton F. M., Fonck R. J., Gammel G. M., Kaita R., Kugel H. W., Powell E. T., Roberts D. W. (1989), Phys. Rev. Lett. **63**, 2060

Seraydarian R. P., Burell K. H., Groebner R. J., (1989) Rev. Sci Instr. **59**, 1530

Soltwisch H. (1992), Plasma Phys. Contr. Fus. **34**, 1669

Summers H. P., Hooper M. B. (1983), Plasma Phys. Contr. Fus. **25**, 1311

Summers H. P., Thomas P., Gianella R., von Hellermann M., Dickson W., Lawson K., Mandl W., Briden P. (1991), Z. Phys. D**21**, 17

Summers H. P., Dickson W. J., Boileau A., Burke P. G., Denne-Hinnov B., Fritsch W., Gianella R., Hawkes N. C., von Hellermann M., Mandl W., Peacock N. J., Reid R. H. G., Stamp M. F., Thomas P. R. (1992), Plasma Phys. Contr. Fus. **34**, 325

Wolle B., Eriksson L. G., Tsintsadze L. N. (1992), submitted to Plasma Phys. Contr. Fus., JET-R(92)02

Wroblewski D., Burrell K. H., Lao L. L., Politzer P., West W. P. (1990), Rev. Sci. Instr. **61**, 3552

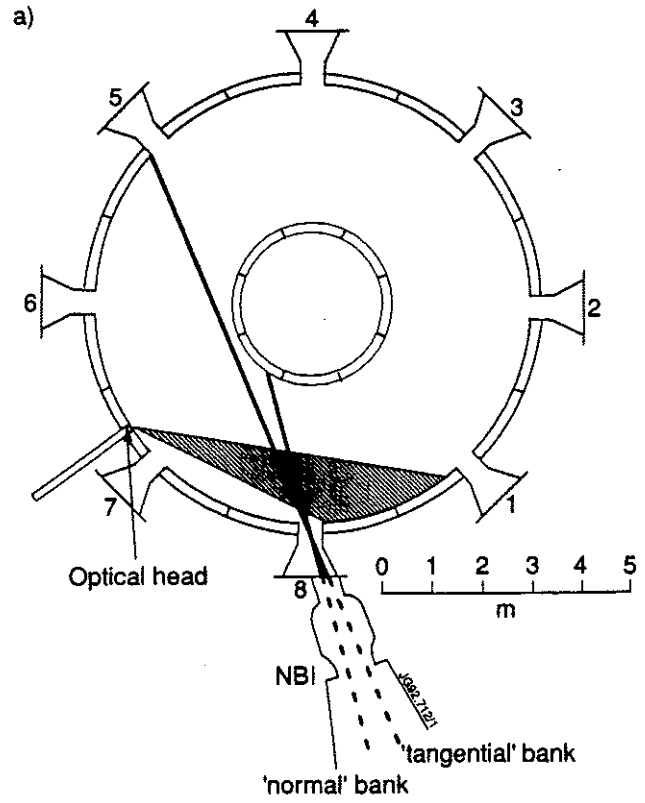

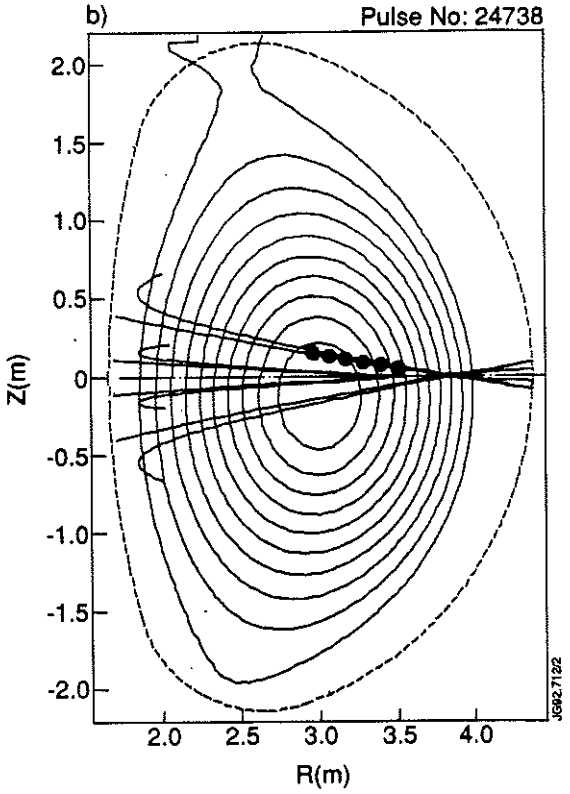

Fig.1: a) Plan view of the JET tokamak showing the neutral beam injector (NBI) assemblies at the torus octant 8. An optical head collects light along a set of nearly horizontal viewing lines intersecting the neutral beams of octant 8. b) Cross-section of the plasma chamber showing the magnetic flux surfaces for a X-point discharge, the projection of the neutral beams and a typical set of observation positions (major radius R, height above the midplane Z).

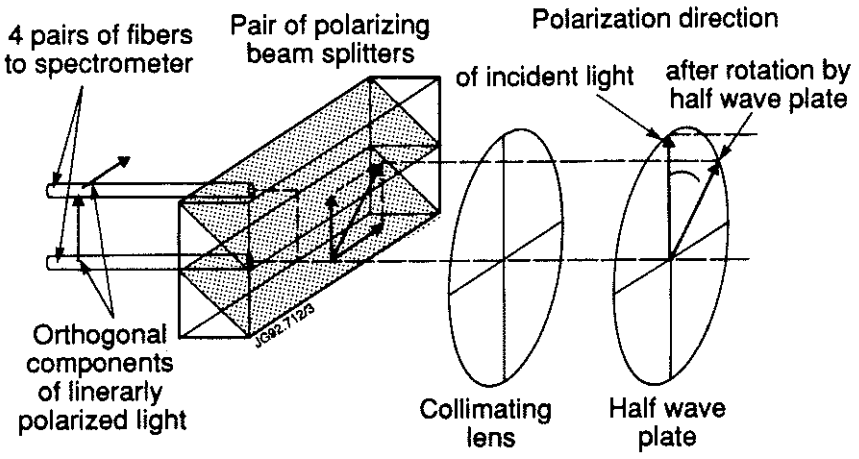

Fig.2: Experimental setup to measure the polarization angles of the Stark multiplet. The polarization plane of the linearly polarized incident light is rotated by a (zero order) half wave plate in order to maximize the sensitivity of the measurement. A collimating lens is used to image different plasma locations onto optical fibers, on top of which an assembly of polarizing beam splitter cubes is mounted. They separate the linearly polarized light into two orthogonal components, each of which gives a full Stark spectrum. With this technique four radial positions are observed simultaneously needing eight detection channels.

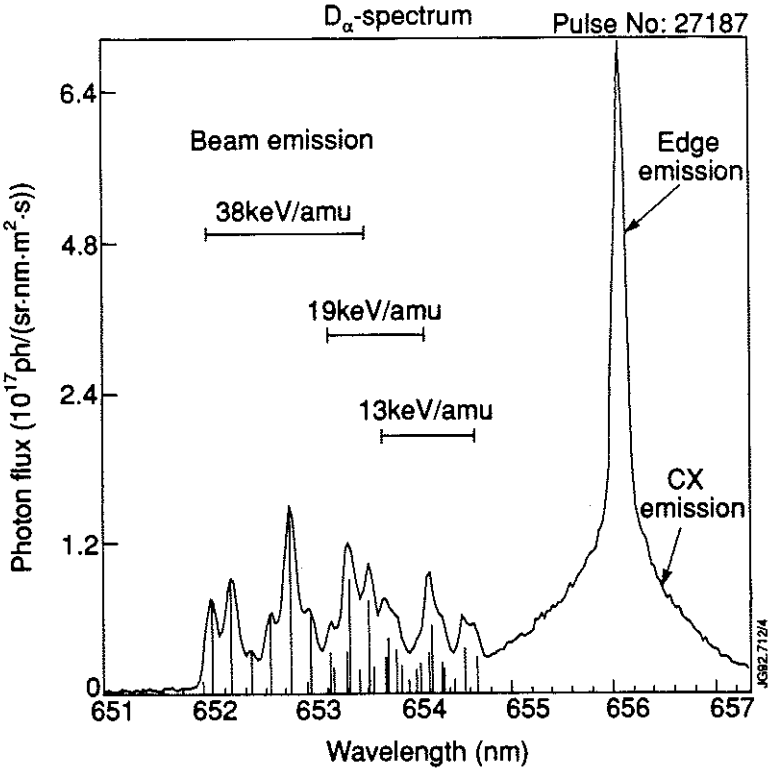

Fig.3: D-α spectrum consisting of edge emission, charge exchange (CX) emission and Doppler shifted beam emission. The beam emission is divided into three energy components. The positions of the individual Stark lines are indicated by vertical bars.

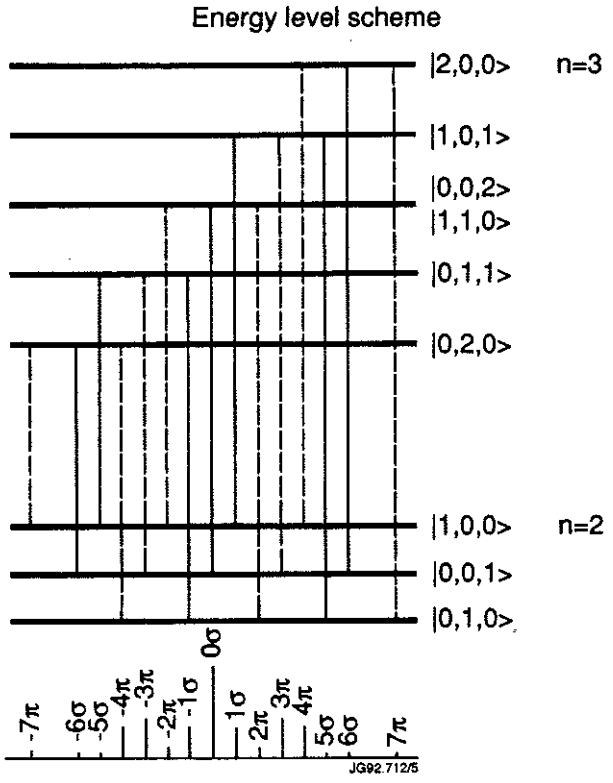

Fig.4: Term diagram of D-α transition and identification of the individual lines in a strong electric field (linear Stark effect) [25]. The ±5σ, ±6σ and ±7π components are more than 2 orders of magnitude weaker than the 0σ component and are therefore usually not observed.

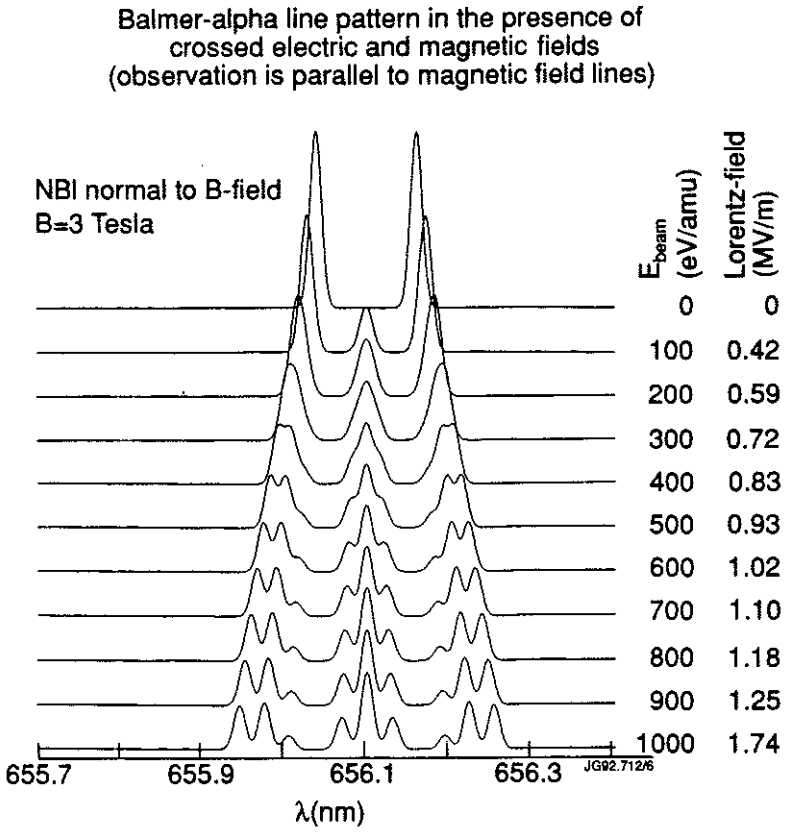

Fig.5a: Transition from Zeeman to Stark line pattern under the influence of an electric $\vec{v}x\vec{B}$ Lorentz field. An arbitrary line width has been used for illustrative purposes.

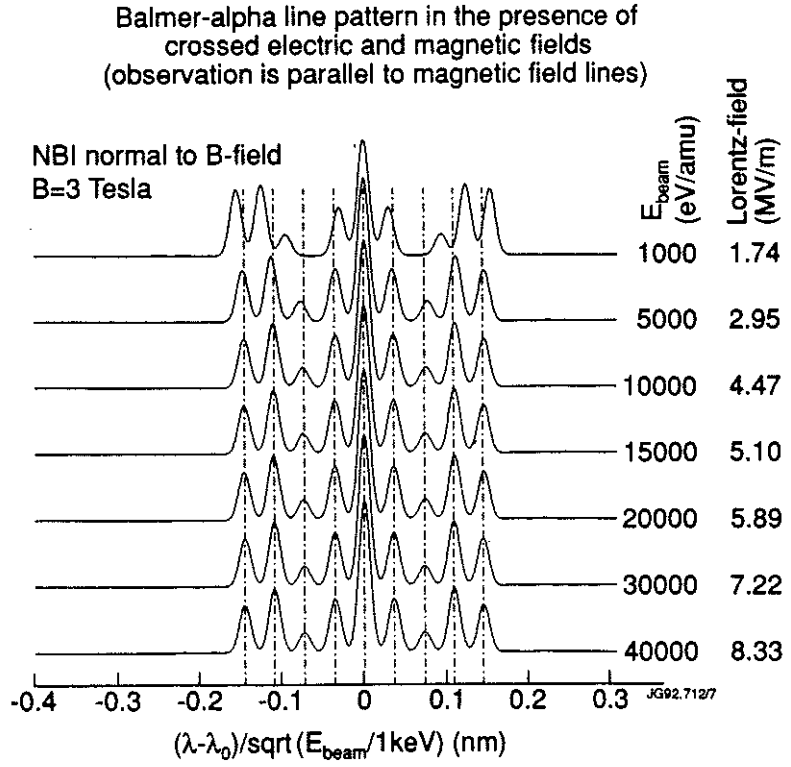

Fig.5b: Deviation of signature of motional Stark effect from the emission pattern of pure Stark effect. An arbitrary line-width has been used for illustrative purposes.

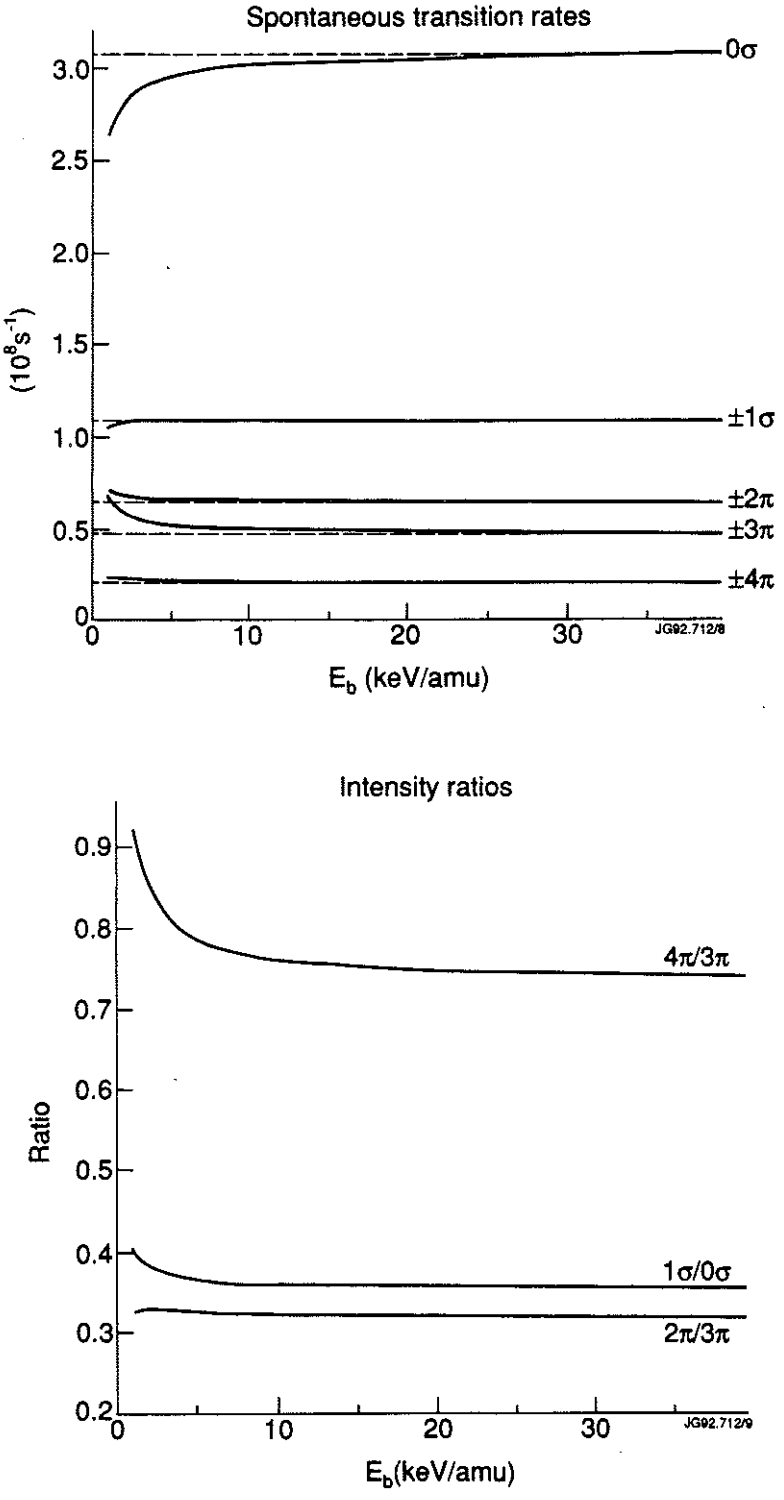

Fig.6, top: Spontaneous transition rates (Einstein coefficients) for the Stark multiplet of the Balmer-alpha transition in hydrogen. B=3 Tesla. A neutral beam is injected perpendicularly to $\vec{B}$, creating a Lorentz electric field $\vec{U}=\vec{v}\times\vec{B}$. The dashed lines indicate the Einstein coefficients for the pure Stark case. Bottom: intensity ratios for some line pairs as a function of neutral beam energy.

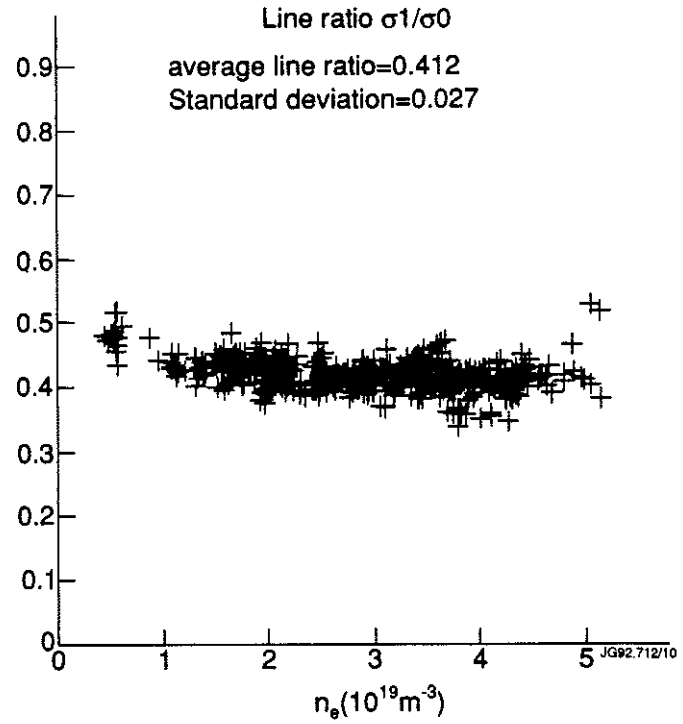
Line ratio σ1/σ0
average line ratio=0.412
Standard deviation=0.027
0.9
0.8
0.7
0.6
0.5
0.4
0.3
0.2
0.1
0
0
1
2
3
4
5
JG92.712/10
$n_e(10^{19}m^{-3})$

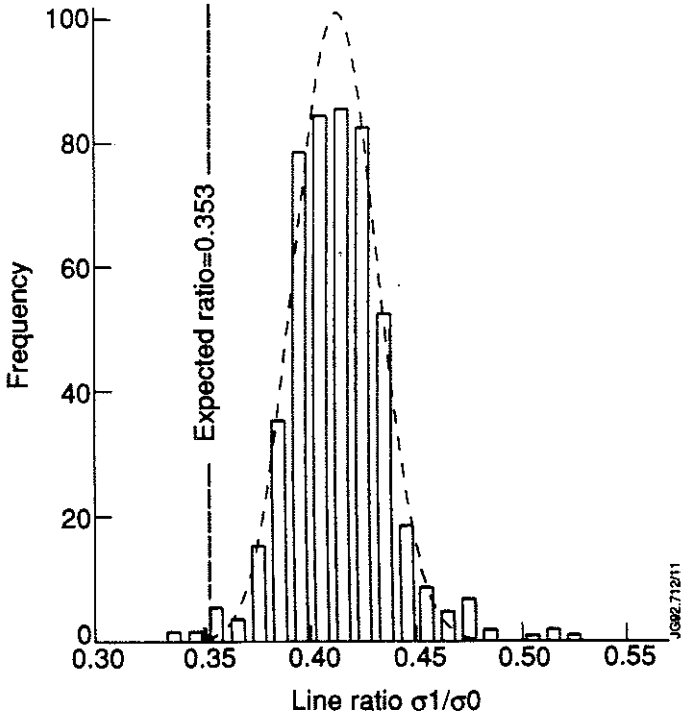
100
80
60
40
20
0
Frequency
Expected ratio=0.353
0.30
0.35
0.40
0.45
0.50
0.55
Line ratio σ1/σ0
JG92.712/11

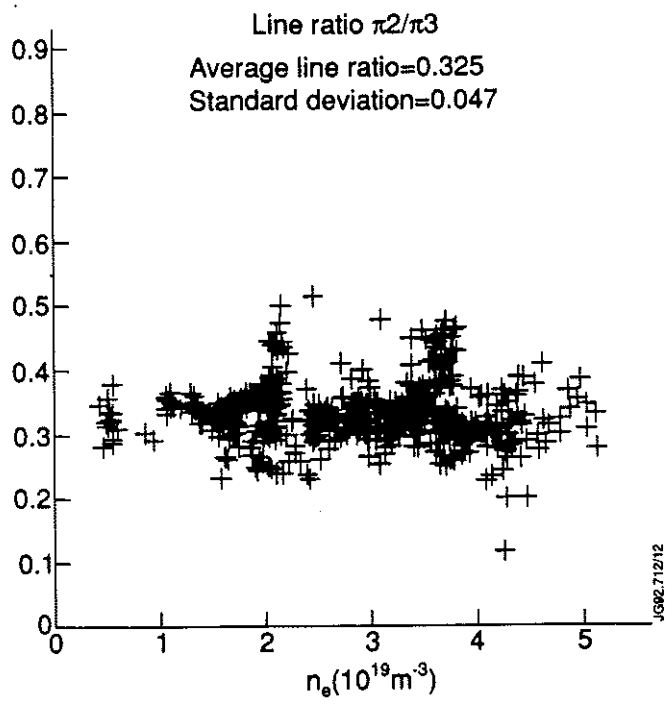
Line ratio π2/π3
Average line ratio=0.325
Standard deviation=0.047
0.9
0.8
0.7
0.6
0.5
0.4
0.3
0.2
0.1
0
0
1
2
3
4
5
$n_e(10^{19}m^{-3})$
JG92.712/12

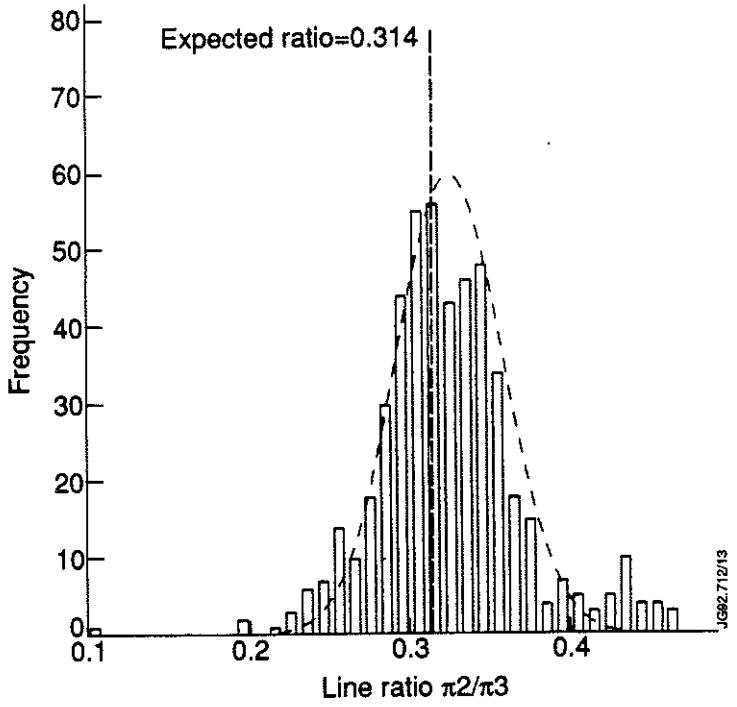
Expected ratio=0.314
80
70
60
50
40
30
20
10
0
Frequency
0.1
0.2
0.3
0.4
Line ratio π2/π3
JG92.712/13

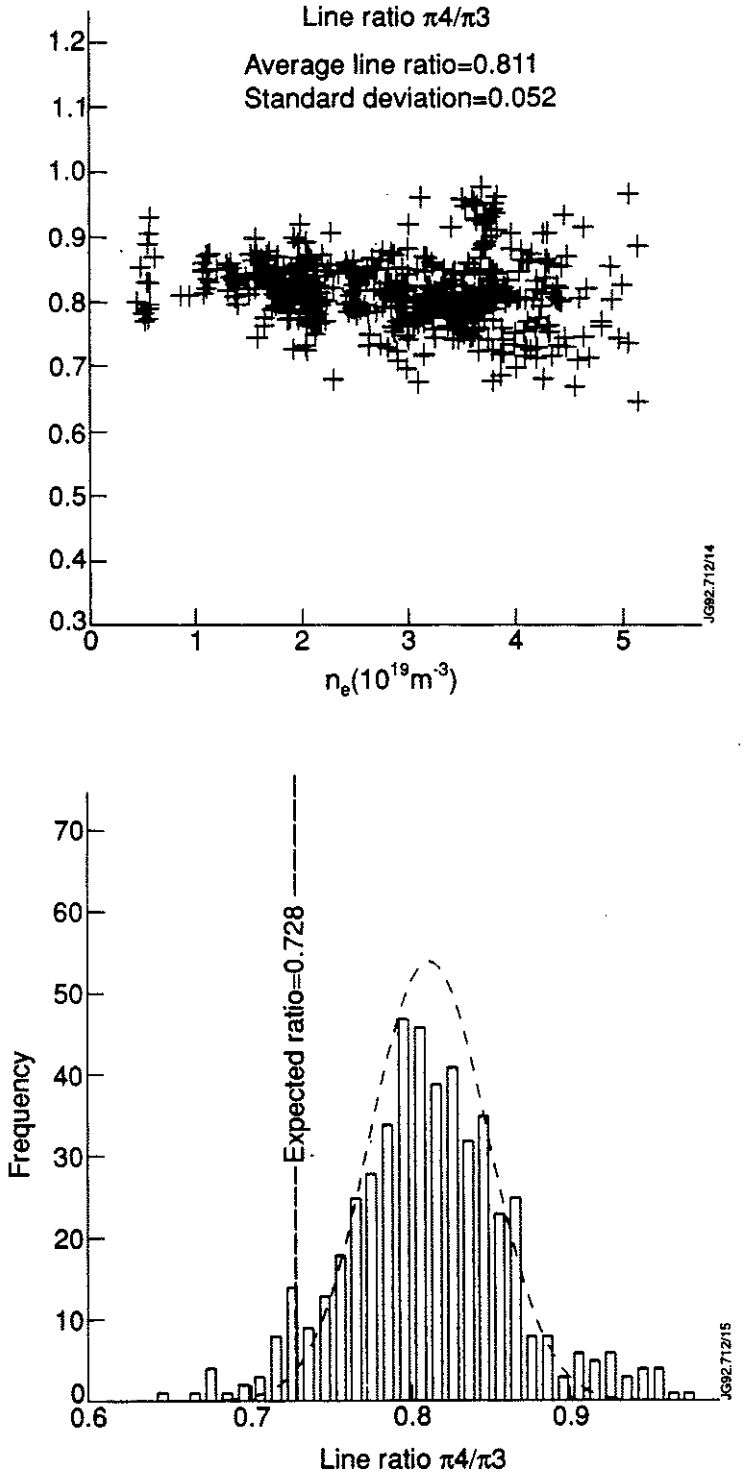

Fig.7: Statistical analysis of line ratios. Only lines within the sigma or within the pi group are compared to avoid geometrical influences. Data of several JET pulses (#19413, #19547, #20057, #20106, #20107), each contributing with radial profiles, are combined here.

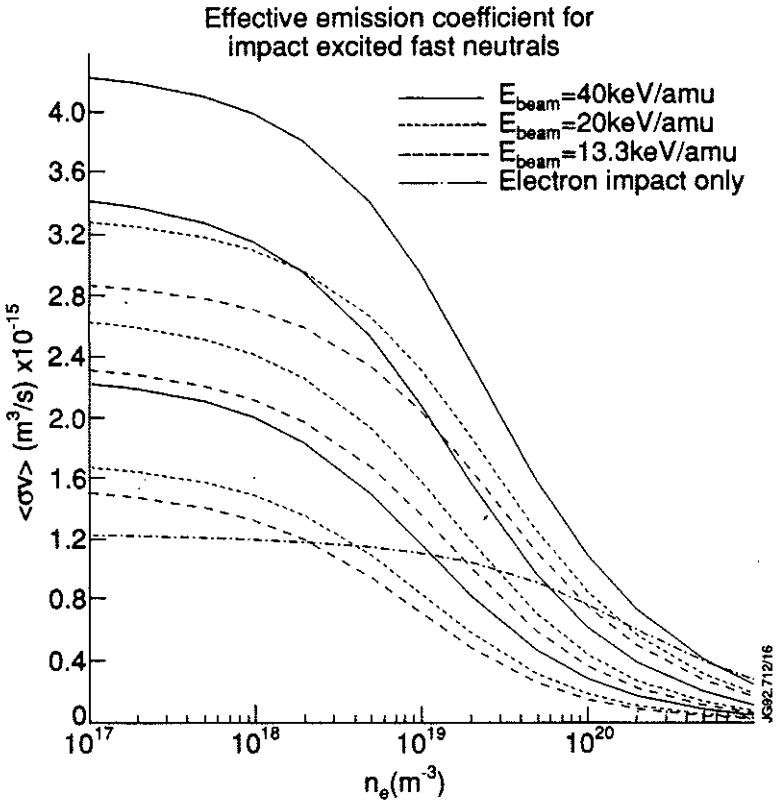

Fig.8a: Balmer-alpha emission coefficients for fast injected neutrals. $T_i=T_e=10keV/k_B$, E_{beam} = 40, 20, and 13.3 keV/amu as indicated. The upper of the three lines corresponding to a given beam energy has been calculated for Z_{eff} = 1, the middle and lower line are for Z_{eff} = 3 and 6. The plasma constituents are deuterium and carbon. For comparison a case where electron impact effects are considered only is shown too.

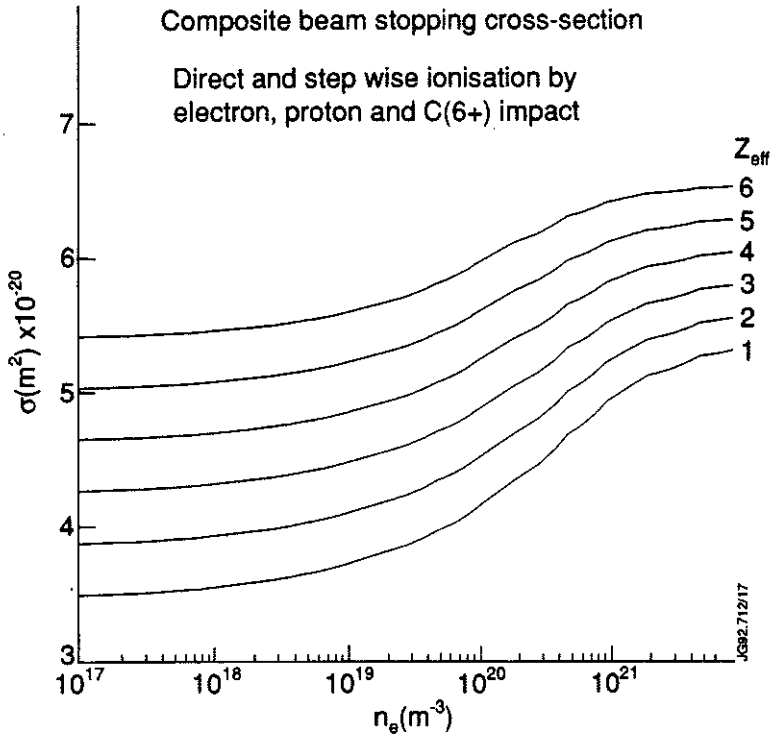

Fig.8b: Enhanced composite beam stopping cross-sections. E_{beam}=40 keV/amu, $T_{ion}=T_{electron}$=10 keV/k_B. The cross-sections have been calculated by means of a collisional-radiative model.

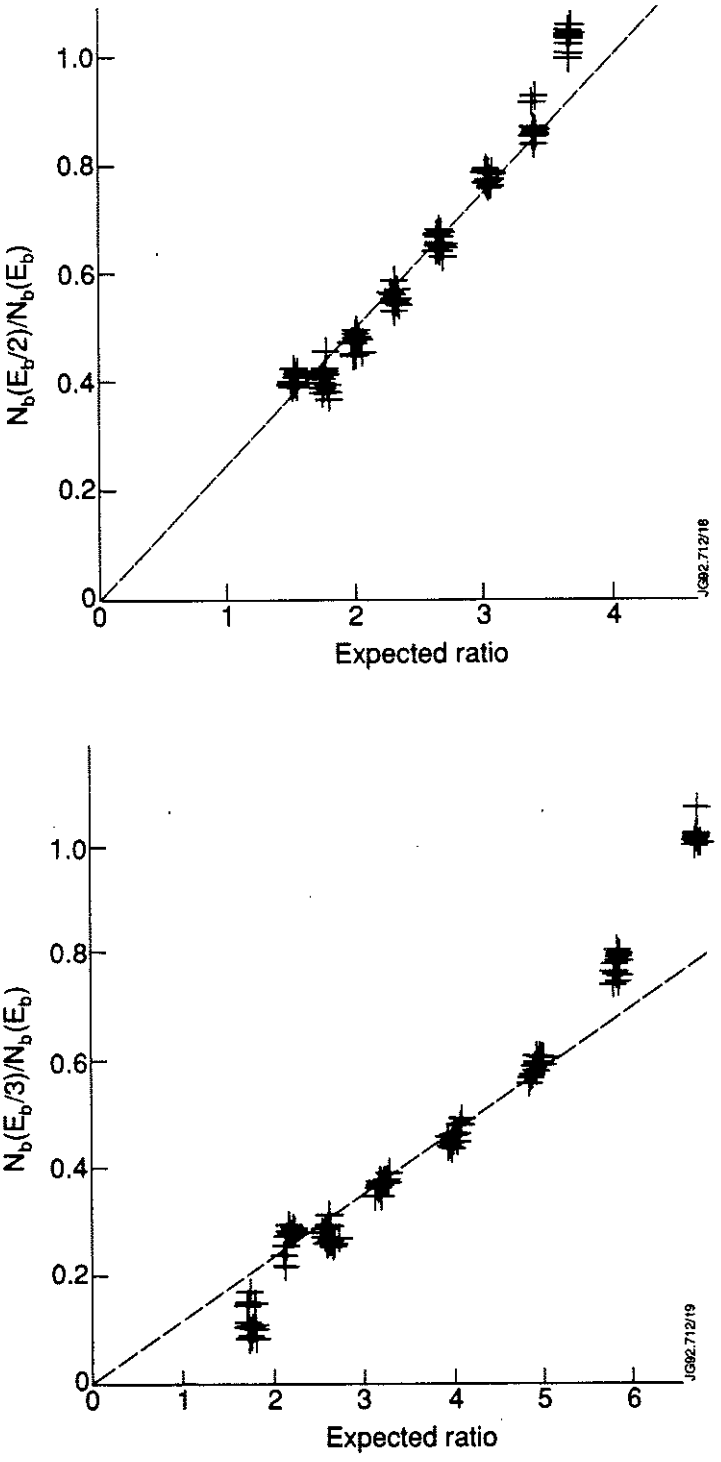

Fig.9: Comparison of relative neutral particle density as evaluated from beam emission spectroscopy and density ratios as calculated using a numerical beam attenuation code. The attenuation calculation is based on the assumption of having the same power input in all the beam fractions. The slope of the graph is therefore a direct measure for the actual power ratio.

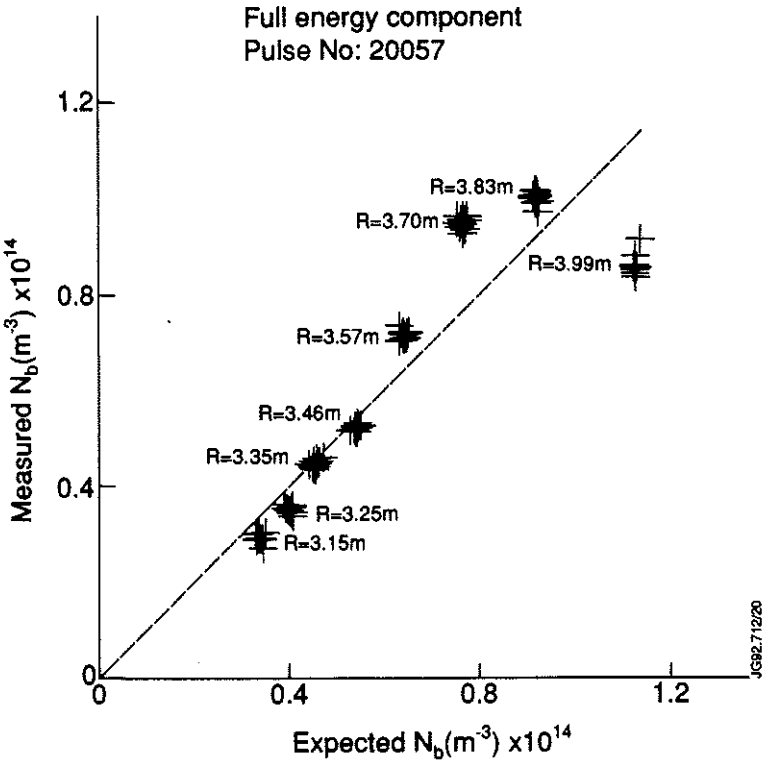

Fig.10: Comparison of local absolute fast neutral particle density from beam emission spectroscopy and beam attenuation code. E_{beam}*=40keV/amu. The observation volumes are located 120 mm below the torus midplane. The radial positions are indicated.*

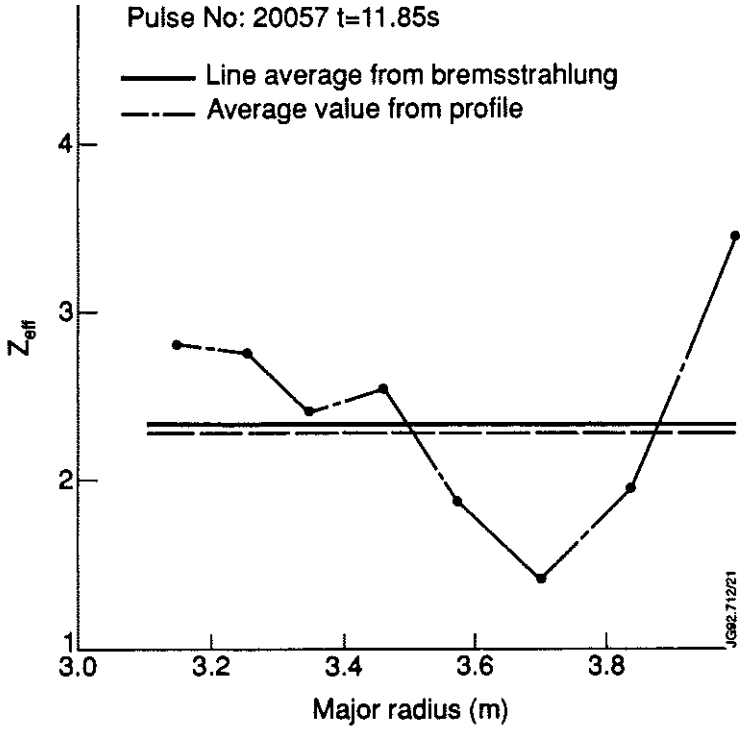

Fig.11: Z_{eff}*-profile, self consistently calculated from measured beam emission and numerically evaluated beam attenuation.*

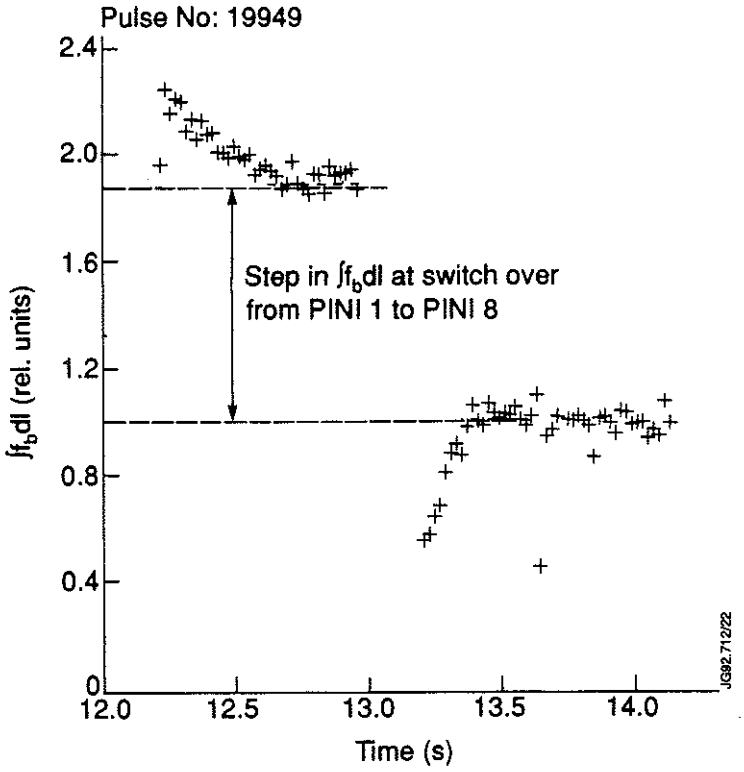

Fig.12: The step in the measured line intensity when neutral beam injection is switched over from pini 1 to pini 8 is due to a change in the line integrated neutral particle density $\int f_b dl$.

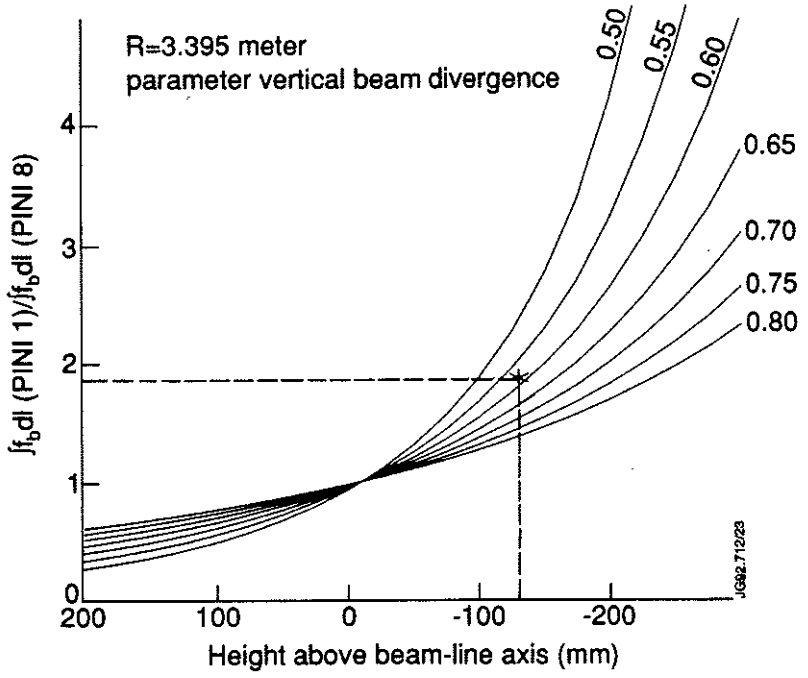

Fig.13: Ratio of the line-integrated neutral particle densities from pini 1 and from pini 8.

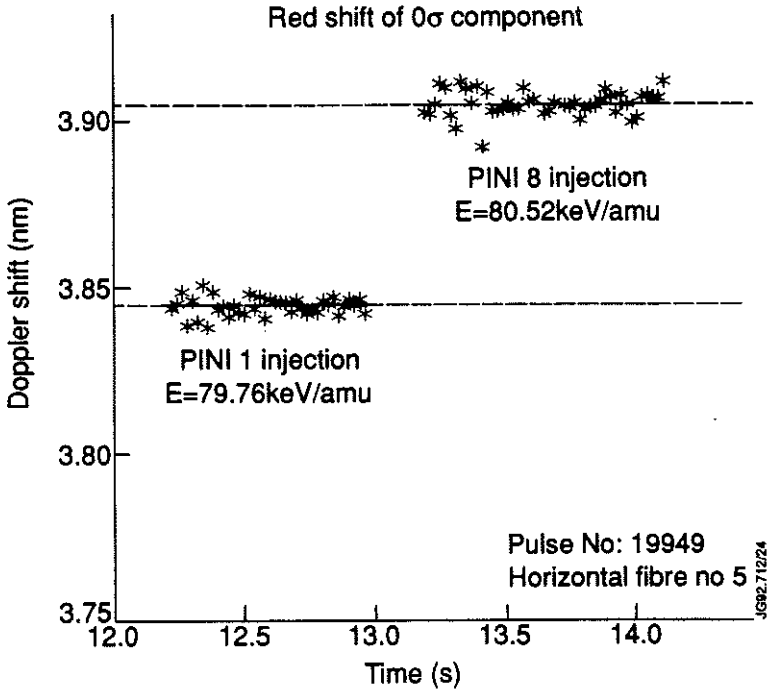

Fig.14: Doppler blue shift of the 0σ-component of the full-energy Stark multiplet as measured in JET pulse #19949 using cord number 5 of the horizontal array of viewing lines. Pini 1 and pini 8 of the octant 8 neutral beam injector box have been fired one at a time each for one second.

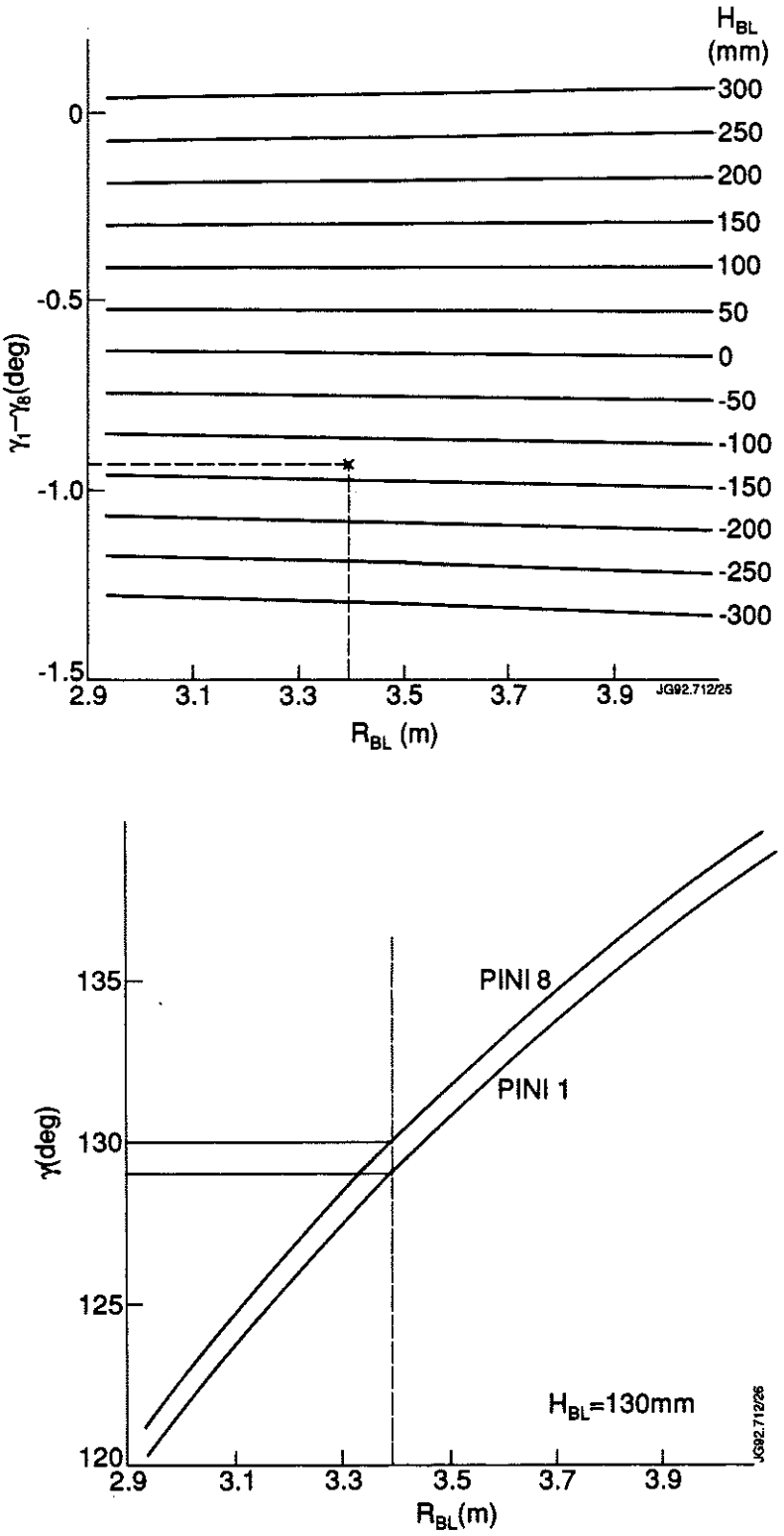

Fig.15: a) Difference $\Delta\gamma=\gamma_8-\gamma_1$ between the intersection angles with respect to pini 1 and 8 as a function of major radius R_{BL} and vertical offset. b) Major radius R_{BL} as a function of the intersection angle γ with respect to neutral particles from pini 1 and from pini 8. The vertical offset H_{BL} is set to -130 mm.

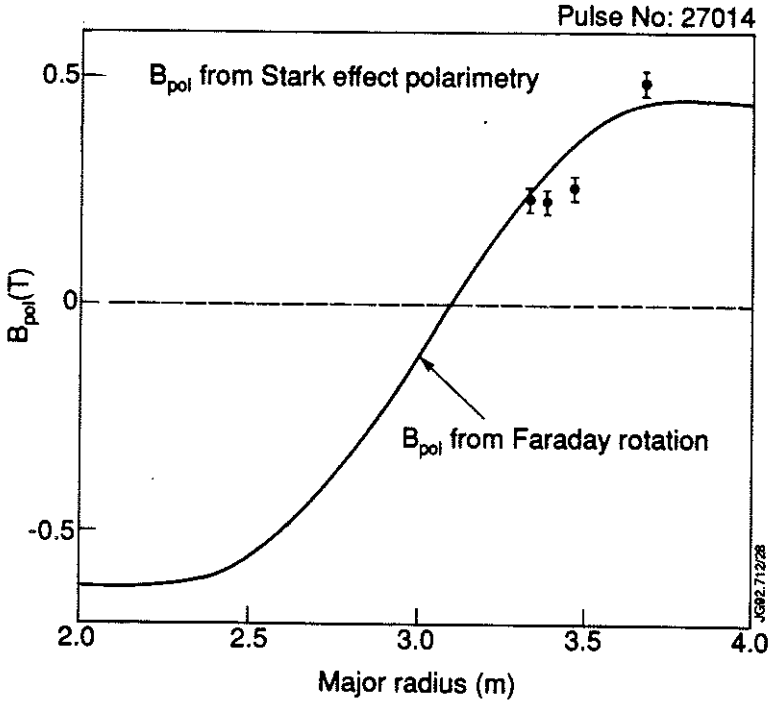

Fig.16: Comparison of the radial poloidal magnetic field profiles. One has been measured with the Stark effect polarimetry, the other one has been obtained by Abel inverting the Faraday rotation angles of the far infrared interferometer. The error bars indicate statistical noise only.

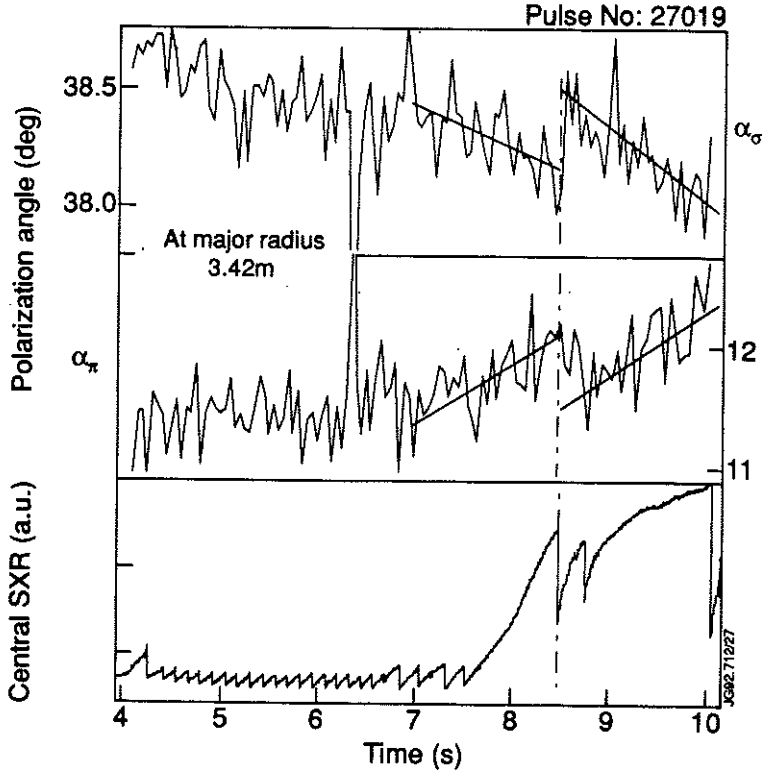

Fig.17: Time evolution of the measured polarization angles from π- and σ-components during a "monster sawtooth" crash. Anti-correlation between the two angles can clearly be seen. The central soft X-ray (SXR) channel shows the evolution of the "sawteeth".

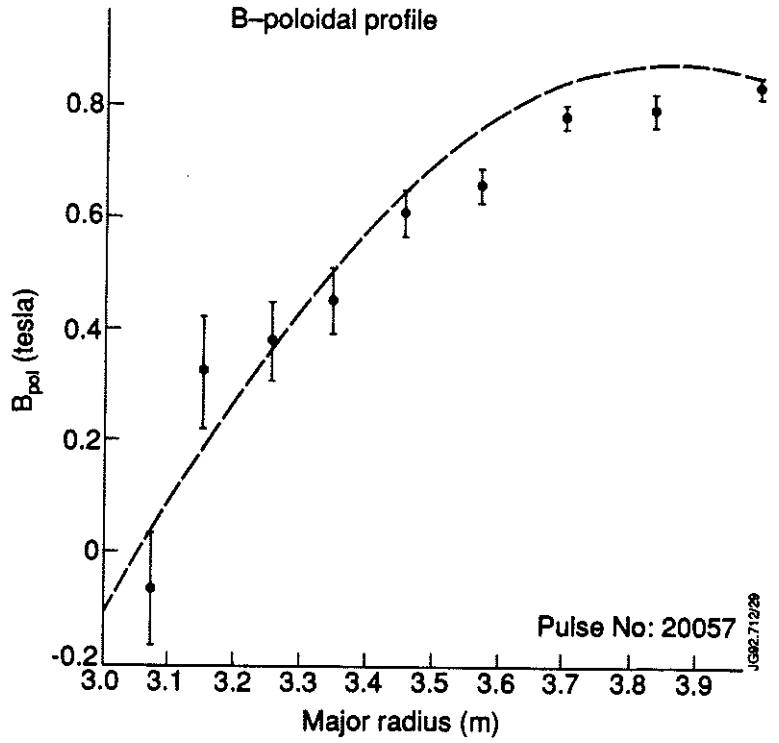

Fig.18: B-poloidal profile measurement using the Stark splitting of the beam components and B-toroidal from a magnetic equilibrium code (IDENTC). The dashed line resembles the calculated B-poloidal profile from the equilibrium code.

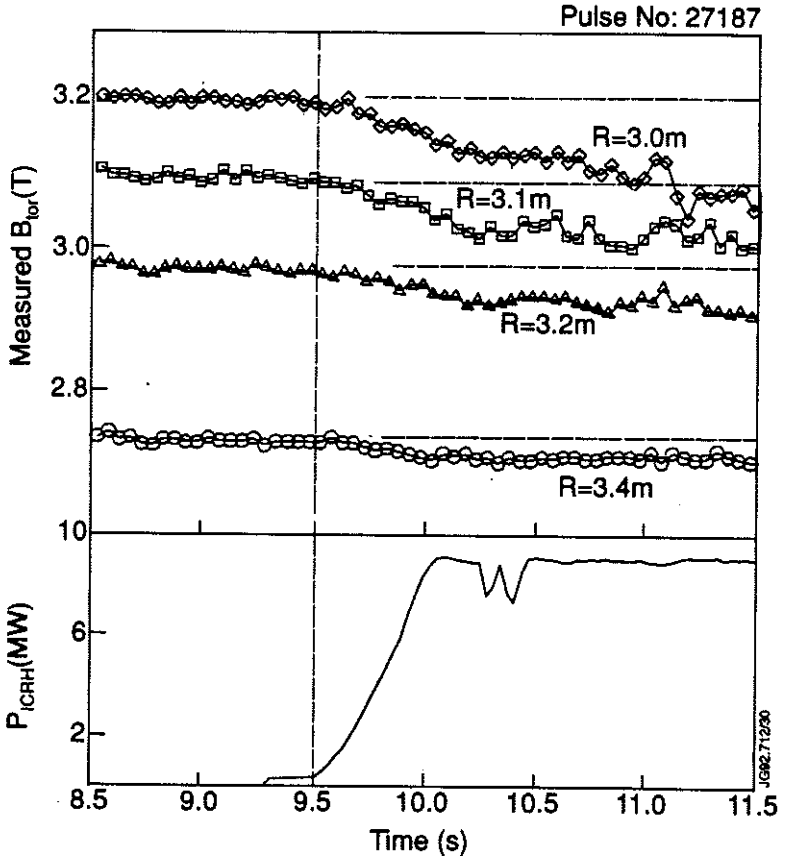

Fig.19: Measured toroidal magnetic field deduced from the Stark splitting in comparison with the ICRH wave form. The ICRH resonance layer is located at about 2.9 m next to the position, where the highest decrease of Btor has been observed.

Appendix I

THE JET TEAM

JET Joint Undertaking, Abingdon, Oxon, OX14 3EA, U.K.

J.M. Adams[1], B. Alper, H. Altmann, A. Andersen[14], P. Andrew, S.Ali-Arshad, W. Bailey, B. Balet, P. Barabaschi, Y. Baranov, P. Barker, R. Barnsley[2], M. Baronian, D.V. Bartlett, A.C. Bell, G. Benali, P. Bertoldi, E. Bertolini, V. Bhatnagar, A.J. Bickley, D. Bond, T. Bonicelli, S.J. Booth, G. Bosia, M. Botman, D. Boucher, P. Boucquey, M. Brandon, P. Breger, H. Brelen, W.J. Brewerton, H. Brinkschulte, T. Brown, M. Brusati, T. Budd, M. Bures, P. Burton, T. Businaro, P. Butcher, H. Buttgereit, C. Caldwell-Nichols, D.J. Campbell, D. Campling, P. Card, G. Celentano, C.D. Challis, A.V.Chankin[23], A. Cherubini, D. Chiron, J. Christiansen, P. Chuilon, R. Claesen, S. Clement, E. Clipsham, J.P. Coad, I.H. Coffey[24], A. Colton, M. Comiskey[4], S. Conroy, M. Cooke, S. Cooper, J.G. Cordey, W. Core, G. Corrigan, S. Corti, A.E. Costley, G. Cottrell, M. Cox[7], P. Crawley, O. Da Costa, N. Davies, S.J. Davies[7], H. de Blank, H. de Esch, L. de Kock, E. Deksnis, N. Deliyanakus, G.B. Denne-Hinnov, G. Deschamps, W.J. Dickson[19], K.J. Dietz, A. Dines, S.L. Dmitrenko, M. Dmitrieva[25], J. Dobbing, N. Dolgetta, S.E. Dorling, P.G. Doyle, D.F. Düchs, H. Duquenoy, A. Edwards, J. Ehrenberg, A. Ekedahl, T. Elevant[11], S.K. Erents[7], L.G. Eriksson, H. Fajemirokun[12], H. Falter, J. Freiling[15], C. Froger, P. Froissard, K. Fullard, M. Gadeberg, A. Galetsas, L. Galbiati, D. Gambier, M. Garribba, P. Gaze, R. Giannella, A. Gibson, R.D. Gill, A. Girard, A. Gondhalekar, D. Goodall[7], C. Gormezano, N.A. Gottardi, C. Gowers, B.J. Green, R. Haange, A. Haigh, C.J. Hancock, P.J. Harbour, N.C. Hawkes[7], N.P. Hawkes[1], P. Haynes[7], J.L. Hemmerich, T. Hender[7], J. Hoekzema, L. Horton, J. How, P.J. Howarth[5], M. Huart, T.P. Hughes[4], M. Huguet, F. Hurd, K. Ida[18], B. Ingram, M. Irving, J. Jacquinot, H. Jaeckel, J.F. Jaeger, G. Janeschitz, Z. Jankowicz[22], O.N. Jarvis, F. Jensen, E.M. Jones, L.P.D.F. Jones, T.T.C. Jones, J-F. Junger, F. Junique, A. Kaye, B.E. Keen, M. Keilhacker, W. Kerner, N.J. Kidd, R. Konig, A. Konstantellos, P. Kupschus, R. Lässer, J.R. Last, B. Laundy, L. Lauro-Taroni, K. Lawson[7], M. Lennholm, J. Lingertat[13], R.N. Litunovski, A. Loarte, R. Lobel, P. Lomas, M. Loughlin, C. Lowry, A.C. Maas[15], B. Macklin, C.F. Maggi[16], G. Magyar, V. Marchese, F. Marcus, J. Mart, D. Martin, E. Martin, R. Martin-Solis[8], P. Massmann, G. Matthews, H. McBryan, G. McCracken[7], P. Meriguet, P. Miele, S.F. Mills, P. Millward, E. Minardi[16], R. Mohanti[17], P.L. Mondino, A. Montvai[3], P. Morgan, H. Morsi, G. Murphy, F. Nave[27], S. Neudatchin[23], G. Newbert, M. Newman, P. Nielsen, P. Noll, W. Obert, D. O'Brien, J. O'Rourke, R. Ostrom, M. Ottaviani, S. Papastergiou, D. Pasini, B. Patel, A. Peacock, N. Peacock[7], R.J.M. Pearce, D. Pearson[12], J.F. Peng[26], R. Pepe de Silva, G. Perinic, C. Perry, M.A. Pick, J. Plancoulaine, J-P. Poffé, R. Pohlchen, F. Porcelli, L. Porte[19], R. Prentice, S. Puppin, S. Putvinskii[23], G. Radford[9], T. Raimondi, M.C. Ramos de Andrade, M. Rapisarda[29], P-H. Rebut, R. Reichle, S. Richards, E. Righi, F. Rimini, A. Rolfe, R.T. Ross, L. Rossi, R. Russ, H.C. Sack, G. Sadler, G. Saibene, J.L. Salanave, G. Sanazzaro, A. Santagiustina, R. Sartori, C. Sborchia, P. Schild, M. Schmid, G. Schmidt[6], H. Schroepf, B. Schunke, S.M. Scott, A. Sibley, R. Simonini, A.C.C. Sips, P. Smeulders, R. Smith, M. Stamp, P. Stangeby[20], D.F. Start, C.A. Steed, D. Stork, P.E. Stott, P. Stubberfield, D. Summers, H. Summers[19], L. Svensson, J.A. Tagle[21], A. Tanga, A. Taroni, C. Terella, A. Tesini, P.R. Thomas, E. Thompson, K. Thomsen, P. Trevalion, B. Tubbing, F. Tibone, H. van der Beken, G. Vlases, M. von Hellermann, T. Wade, C. Walker, D. Ward, M.L. Watkins, M.J. Watson, S. Weber[10], J. Wesson, T.J. Wijnands, J. Wilks, D. Wilson, T. Winkel, R. Wolf, D. Wong, C. Woodward, M. Wykes, I.D. Young, L. Zannelli, A. Zolfaghari[28], G. Zullo, W. Zwingmann.

PERMANENT ADDRESSES

1. UKAEA, Harwell, Didcot, Oxon, UK.
2. University of Leicester, Leicester, UK.
3. Central Research Institute for Physics, Budapest, Hungary.
4. University of Essex, Colchester, UK.
5. University of Birmingham, Birmingham, UK.
6. Princeton Plasma Physics Laboratory, New Jersey, USA.
7. UKAEA Culham Laboratory, Abingdon, Oxon, UK.
8. Universidad Complutense de Madrid, Spain.
9. Institute of Mathematics, University of Oxford, UK.
10. Freien Universität, Berlin, F.R.G.
11. Royal Institute of Technology, Stockholm, Sweden.
12. Imperial College, University of London, UK.
13. Max Planck Institut für Plasmaphysik, Garching, FRG.
14. Risø National Laboratory, Denmark.
15. FOM Instituut voor Plasmafysica, Nieuwegein, The Netherlands.
16. Dipartimento di Fisica, University of Milan, Milano, Italy.
17. North Carolina State University, Raleigh, NC, USA
18. National Institute for Fusion Science, Nagoya, Japan.
19. University of Strathclyde, 107 Rottenrow, Glasgow, UK.
20. Institute for Aerospace Studies, University of Toronto, Ontario, Canada.
21. CIEMAT, Madrid, Spain.
22. Institute for Nuclear Studies, Otwock-Swierk, Poland.
23. Kurchatov Institute of Atomic Energy, Moscow, USSR
24. Queens University, Belfast, UK.
25. Keldysh Institute of Applied Mathematics, Moscow, USSR.
26. Institute of Plasma Physics, Academica Sinica, Hefei, P. R. China.
27. LNETI, Savacem, Portugal.
28. Plasma Fusion Center, M.I.T., Boston, USA.
29. ENEA, Frascati, Italy.

At 1st July, 1992